AGU PUBLICATIONS

JGR

Journal of Geophysical Research: Solid Earth

RESEARCH ARTICLE
10.1002/2013JB010607

Key Points:
- Relief in the western Cordillera is dominantly crustal in origin
- No dynamic topography is needed away from subduction zone
- Gravitational potential energy anomalies encourage modern strain

Supporting Information:
- Readme
- Table S1

Correspondence to:
W. Levandowski,
will.levandowski@colorado.edu

Citation:
Levandowski, W., C. H. Jones, W. Shen, M. H. Ritzwoller, and V. Schulte-Pelkum (2014), Origins of topography in the western U.S.: Mapping crustal and upper mantle density variations using a uniform seismic velocity model, *J. Geophys. Res. Solid Earth*, *119*, 2375–2396, doi:10.1002/2013JB010607.

Received 14 AUG 2013
Accepted 21 JAN 2014
Accepted article online 20 JAN 2014
Published online 12 MAR 2014

Origins of topography in the western U.S.: Mapping crustal and upper mantle density variations using a uniform seismic velocity model

Will Levandowski[1], Craig H. Jones[1], Weisen Shen[2], Michael H. Ritzwoller[2], and Vera Schulte-Pelkum[1]

[1]Cooperative Institute for Research in Environmental Sciences and Department of Geological Sciences, University of Colorado Boulder, Boulder, Colorado, USA, [2]Department of Physics, University of Colorado Boulder, Boulder, Colorado, USA

Abstract To investigate the physical basis for support of topography in the western U.S., we construct a subcontinent scale, 3-D density model using ~1000 estimated crustal thicknesses and *S* velocity profiles to 150 km depth at each of 947 seismic stations. Crustal temperature and composition are considered, but we assume that mantle velocity variations are thermal in origin. From these densities, we calculate crustal and mantle topographic contributions. Typical 2σ uncertainty of topography is ~500 m, and elevations in 84% of the region are reproduced within error. Remaining deviations from observed elevations are attributed to melt, variations in crustal quartz content, and dynamic topography; compositional variations in the mantle, while plausible, are not necessary to reproduce topography. Support for western U.S. topography is heterogeneous, with each province having a unique combination of mechanisms. Topography due to mantle buoyancy is nearly constant (within ~250 m) across the Cordillera; relief there (>2 km) results from variations in crustal chemistry and thickness. Cold mantle provides ~1.5 km of ballast to the thick crust of the Great Plains and Wyoming craton. Crustal temperature variations and dynamic pressures have smaller magnitude and/or more localized impacts. Positive gravitational potential energy (GPE) anomalies ($\sim 2 \times 10^{12}$N/m) calculated from our model promote extension in the northern Basin and Range and near the Sierra Nevada. Negative GPE anomalies (-3×10^{12}N/m) along the western North American margin and Yakima fold and thrust belt add compressive stresses. Stresses derived from lithospheric density variations may strongly modulate tectonic stresses in the western U.S. continental interior.

1. Introduction

The Cordilleran orogen of the western United States is one of the broadest on Earth. Elevations above 2 km extend 1500 km from the plate boundary (Figure 1a) and active deformation extends 1000 km from the plate boundary. Unlike other relatively broad boundaries, this orogen lacks a continental collision or even subduction over much of its length. The processes producing such widespread uplift and deformation remain poorly understood largely because of the heterogeneous history of different parts of the orogen and the absence of uniformly collected and analyzed orogen-scale information on crustal and upper mantle structure. We address this deficiency through analysis of newly created seismic wave speed models developed from ambient noise and earthquake surface wave observations at EarthScope Transportable Array (TA) stations spaced roughly every 80 km throughout the region.

Variations in continental elevation stem from some combination of variations in crustal density, crustal thickness, mantle density, and basal normal stress at the model bottom, to the last of which we apply the unevenly defined term "dynamic topography." The mantle component of topography arises from variations in the density and thickness of the mantle lithosphere. Variations in the thickness of crust and mantle lithosphere are generally products of tectonism, whereas variations in densities are often the results of magmatism and thermal adjustments that can occur during more tectonically quiescent times. Thus, isolating the modern day mechanisms of support for provinces within the western U.S. contributes toward our understanding of the tectonic evolution of the continental lithosphere.

At the broadest scale, the elevation of the orogen is often attributed to a warm and buoyant mantle [e.g., *Grand and Helmberger*, 1984] emplaced after removal of the lower lithosphere because of "flat slab" subduction during the 75–45 Ma Laramide orogeny [e.g., *Bird*, 1988; *Spencer*, 1996; *Humphreys*, 2009]. Challenges to this model range from disagreements over the geometry of the Laramide-age slab [e.g., *Sigloch and*

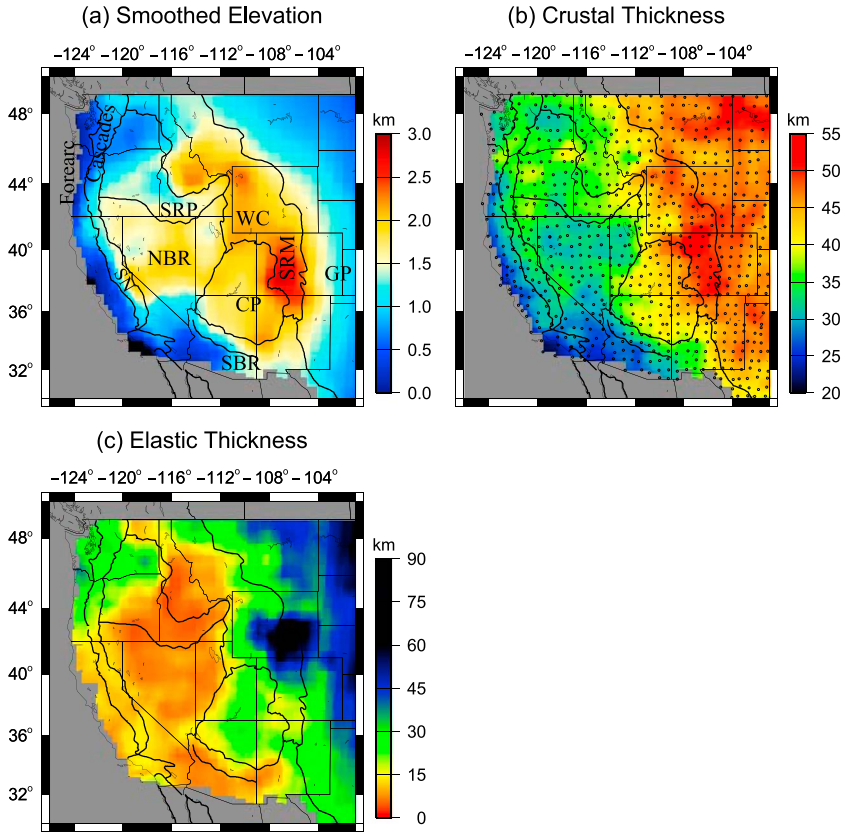

Figure 1. (a) Elevation of the western U.S., smoothed as discussed in the text. Physiographic boundaries are shown in black outline. SN: Sierra Nevada, SRP: Snake River Plain, NBR: northern Basin and Range, SBR: southern Basin and Range, CP: Colorado Plateau, SRM: Southern Rocky Mountains, WC: Wyoming craton, and GP: Great Plains. (b) Crustal thicknesses from *Shen et al.* [2013a]. Each of the 947 seismic stations used is marked with a small circle. (c) Elastic thickness estimated from *Lowry* [2012].

Mihalynuk, 2013; *Saleeby*, 2003] through the post-Laramide presence of pre-Laramide mantle lithosphere in the western U.S. [e.g., *Livaccari and Perry*, 1993; *Ducea and Saleeby*, 1996] to unexplained >1 km modern elevations of the untectonized High Plains [*Eaton*, 1986]. As a result, many workers have chosen to focus on pieces of the orogen, introducing a broad range of mechanisms for surface uplift of portions of the region. In the Colorado Plateau, for example, *Roy et al.* [2009] argue that ~2 km of Cenozoic surface uplift is due to conductive warming of the lithosphere, *Levander et al.* [2011] attribute elevation change to delamination of the lower crust and mantle lithosphere, and *Moucha et al.* [2008] and *Liu and Gurnis* [2010] favor dynamic support from the mantle convective regime. Such province-scale studies often lack a regional framework to contextualize and substantiate hypotheses. In this study, we provide such a framework and illustrate its application with specific examples.

The presence of Pleistocene to Recent deformation ~1000 km from the Pacific plate potentially shares a common origin with topography. The variations in stress manifest in observed strain are typically attributed to lateral variations in gravitational potential energy that arise from lateral variations in the thickness, elevation, and density of the lithosphere [e.g., *Flesch et al.*, 2000, 2007; *Humphreys and Coblentz*, 2007; *Sonder and Jones*, 1999], although the significance of the stresses generated by gravitational potential energy (GPE) variations has been disputed [*Parsons and Thatcher*, 2011]. Previous estimates of GPE (and thus the stresses that arise from lateral GPE variations) relied either on filtering geoid anomalies or compiling and interpolating seismic models produced by different techniques and then converting such structures into density. Geoid anomalies are equivalent to GPE if all the density anomalies contributing to the geoid are within the depth range appropriate for GPE calculations [*Haxby and Turcotte*, 1978]. In the western U.S., however, a long wavelength contribution is probably sublithospheric, so most workers filter the geoid [e.g., *Flesch et al.*, 2000; *Jones et al.*, 1996]. Although filtering removes the deeper contributions, it also can remove longer wavelength

(e.g., province-scale) shallow contributions. Compiling seismic models in the literature and converting these to GPE estimates [e.g., *Jones et al*., 1996] carry the risk that biases between different workers and techniques will create geographic biases in GPE estimates. For many geodynamic applications, these discrete seismic models must be interpolated in some manner (e.g., CRUST 2.0, as used, for instance, by *Flesch and Kreemer* [2010]) that can further amplify biases and errors. A uniformly calculated estimate of GPE derived from an evenly distributed set of seismic observations would, at minimum, reduce any intraorogenic uncertainty due to these biases.

The motivation for this work is to leverage the passage of Transportable Array (TA) seismometers across the western U.S. (Figure 1a) and the development of new seismic techniques [*Shen et al*., 2013b] to produce a spatially pseudouniform 3-D density model across the entire western U.S. The distribution of accepted velocity models (detailed below) provided by *Shen et al*. [2013a] removes interinvestigator biases while providing a robust measure of seismological uncertainty. In turn, the envelope of densities estimated from those velocities allows us to quantify the mechanisms of modern topographic support and decompose this field into crustal and mantle or thermal and compositional components. Finally, the density estimates consistent with topography and seismic velocities determine variations in the body forces that contribute to the modern stress field. This workflow overcomes many of the challenges faced in previous studies, which had to rely upon spatially variable data coverage, nonuniform data processing techniques, and models that may be highly dependent on the chosen inversion parameters.

Such an improved model set allows us to pursue answers to technically and geodynamically important questions. Can seismic velocities, in concert with heat flow measurements, be used to reliably estimate densities? We check our density estimates quantitatively against predicted topography and gravity. Where do these predictions fail? We examine regions where dynamic topography, crustal melt, and anomalously felsic crust are likely. To what extent are thermal, compositional, and dynamic topography each responsible for surface elevations, and is one dominant? We decompose the elevation field into these components. What are the magnitudes of GPE variations in the western U.S., and how do these variations compare with modern strain? We quantify the GPE with respect to the asthenosphere throughout the region. For use in future work, we include an electronic supplement that contains our estimated parameters at each station.

2. Seismic Models

The passage of the Transportable Array across the western U.S. has allowed pseudouniform seismic coverage of the region and new processing techniques have allowed for more robust interpretation of the data in terms of seismic wave speed and lithospheric structure. The models thus derived represent a tool that was unavailable to previous workers, who had to rely upon velocity structures available at the time. Ideally, models would sample the lithosphere uniformly and could distinguish wave speeds in the crust from those in the mantle, as the relationship of wave speed to density differs in the two layers.

Shen et al. [2013b] present a technique that creates velocity models of unprecedented utility in calculating the buoyancy of crustal and mantle components in that it (1) generates uniformly sampled and processed velocity models to 150 km depth and with ~100 km lateral resolution, (2) includes crustal thickness constraints, and (3) allows easy tracking of uncertainty. At each of 947 TA stations in the western U.S., *Shen et al*. [2013a] began with a loosely constrained prior distribution of seismic V_{SV} velocities with depth and derived posterior distributions of ~1000 shear wave velocity profiles (0–150 km; Figure 2d) and crustal thicknesses (mean shown in Figure 1b) that jointly satisfy surface wave dispersion curves and receiver functions. The entire posterior distribution of (acceptable) velocity profiles can be used in later calculations, allowing robust tracking of uncertainty (Figure 2). The inclusion of receiver function constraints greatly improves depth resolution of velocities when compared to surface wave dispersion simulations alone [*Shen et al*., 2013b].

The models derived from this technique offer advantages over those previously available for investigations of lithospheric density and buoyancy, which were primarily derived from active-source profile, surface tomography, local earthquake tomography, or teleseismic body wave tomography. Active-source profiles are necessarily scattered, and interpretations, particularly of secondary arrivals, frequently differ between different workers (e.g., contrast *Holbrook* [1990] with *Catchings and Mooney* [1991] or *Prodehl* [1979] with *Wolf and Cipar* [1993]). Further, while quite powerful in resolving crustal velocity, these models rarely extend into

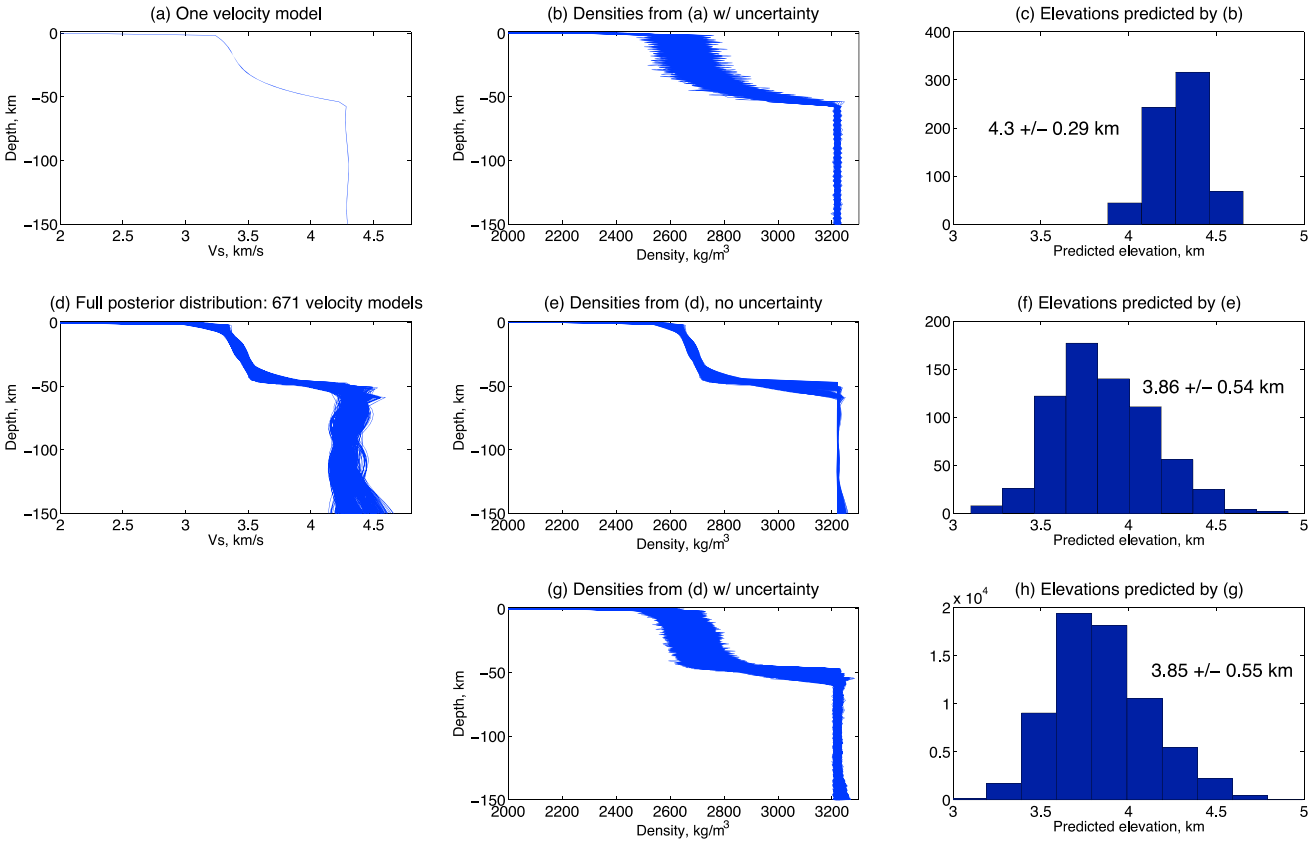

Figure 2. (a) A single member of the posterior distribution of *S* velocity profiles for station S22A, Creede, CO. (b) The envelope of 671 density profiles derived from Figure 2a, with random error in velocity-density conversion at each node as given by *Christensen and Mooney* [1995] in the crust and with 30% uncertainty in the mantle. Uncertainty is not vertically correlated. (c) Histogram of the elevations predicted from Figure 2b. Uncertainty is 2σ. (d) The 671 *S* velocity profiles in the posterior distribution at station S22A. (e) The envelope of densities derived from Figure 2d, with no uncertainty in velocity-density conversion. (f) Histogram of the elevations predicted from Figure 2e. Note different mean and much larger uncertainty than Figure 2c. (g) The envelope of densities derived from Figure 2d, but with uncertainty as in Figure 2b. (h) Histogram of elevations predicted from Figure 2g. Note similar mean and uncertainty to Figure 2f.

the mantle lithosphere. Surface wave models have more uniformly sampled the lithosphere in this region with the deployment of the TA, but trade-offs between wave speeds of the crust and mantle are typically large. Local earthquake tomography is possible only where events occur and typically has poor resolution at depths in the upper mantle and lower crust below the deepest events. Teleseismic body wave tomography and receiver functions recover only lateral gradients or contrasts and not absolute values and typically contain little information within the crust.

Because *Shen et al*. [2013a] produce a distribution of posterior models that satisfy the original observations, we can properly account for the effect of uncertainty in the seismological models on the derived density profile (Figures 2e and 2g). Previous work often relied on forward modeling of seismic traveltime observations lacking formal estimates of uncertainty. Additionally, because wave speed structures intrinsically carry tradeoffs between different depths (that is, uncertainties at one depth will covary with those at other depths), by estimating derived parameters (such as mean density) for each individual structure and then calculating the uncertainty in the derived parameter, we avoid overestimating the uncertainties arising from the seismological uncertainties. As explained in greater detail in section 4, we find that this seismological uncertainty dominates the uncertainty in our predicted topography, exceeding the uncertainty from the scatter in velocity to density regressions (Figure 2).

3. Density Estimation and Decomposition of Topography

We investigate the source of topographic relief in the western U.S. by exploiting the relationship between wave speed and density. It is useful to separate the contribution to topography (ε) from the crust

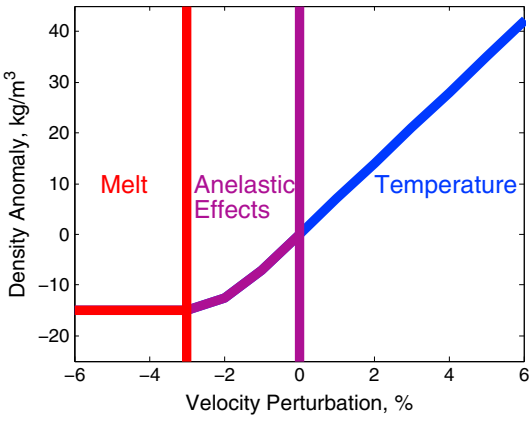

Figure 3. Mantle velocity-density relationship based on purely thermal effects. At low temperatures (positive velocity perturbations relative to 4.5 km/s), the relationship is linear with a slope of 7 kg/m^3 per 1% velocity difference (~70°C). Between 0% and −3% (~150°C heating) velocity perturbation, anelastic effects begin to dominate, augmenting the velocity decrease for a unit temperature increase while density is still a linear function of temperature. At velocities lower than −3% (greater than 150°C above background), we assume that material is above the solidus. Increased thermal input produces more melt, lowering velocity further, while melt has a very similar density to rock of the same temperature and thus bulk density remains constant [*Hammond and Humphreys*, 2000].

(H_c) from that from the mantle (H_m). In this, we follow *Lachenbruch and Morgan* [1990] and define the following:

$$\varepsilon = H_c + H_m - H_0 \tag{1}$$

where the crustal and mantle contributions to buoyant height are

$$H_c = \int_{-\varepsilon}^{z_c} \frac{\rho_a - \rho(z)}{\rho_a} dz$$
$$H_m = \int_{z_c}^{z_a} \frac{\rho_a - \rho(z)}{\rho_a} dz \tag{2}$$

H_0 is a correction term of 2.4 km to achieve isostatic equilibrium with an asthenospheric column (via mid-ocean ridges). z is positive downward, such that the depth of the Moho below sea level is z_c. We assume the asthenosphere to be laterally uniform below the base of the seismic models (z_a) at 150 km, and we discuss the biases introduced by this assumption below. The density of the asthenosphere, ρ_a, is assumed to be 3200 kg/m^3. Because the motivation of this study is to explore the source of topographic variation in the region, the exact choice of reference asthenospheric density is of second-order importance. ε is the isostatically supported elevation above sea level, or the convolution of surface elevation with the flexural filter of the lithosphere (e.g., following *Jones et al.* [1996]). This convolution, in essence a low-pass filtering of surface elevation, removes flexurally supported topography from ε. The filter is a zero-order Bessel function [*Watts*, 2001] appropriate for elastic thickness estimates at each station (Figure 1c) [*Lowry et al.*, 2000; *Lowry*, 2012]. A model of isostatic and dynamic buoyancy is viable if, when convolved with this same filter, it reproduces this smoothed elevation within uncertainty.

In order to calculate H_m and H_c, at each point we convert each of the ~1000 members of the distribution of v_s models into a density profile. Separating the support for smoothed topography into crustal and mantle components is necessary because we use different approaches in crust and mantle to derive densities from seismic wave speeds. The crustal and mantle topographic contributions are smoothed by the same flexural filter described above to produce an estimate of the surface expression of these loads.

3.1. Mantle-Supported Topography

We initially solve for H_m (which we will term the mantle topography for clarity) by assuming that density and wave speed variations are a product of thermal heterogeneity. Isobaric heating will produce a decrease in both density and seismic velocity. Over a wide variety of lherzolite, harzburgite, and peridotite mineralogies the temperature derivative of density is nearly the same, though the absolute densities vary considerably [*Hacker and Abers*, 2004]. Therefore, we make no initial assumption of mantle mineralogy other than that it is laterally constant across the study area at any depth. This simplification is clearly not a robust characterization of the lithosphere and upper asthenosphere, so we will later examine regions where compositional variations may manifest themselves as residuals in topography and gravity calculated assuming uniform mineralogy. Converting velocity anomalies to density anomalies, we can then constrain the mantle contributions to isostasy for a purely thermally varying mantle, interpreting *S* wave speed variations reported by *Shen et al.* [2013a] as temperature variations and calculating the resulting density structure.

Laboratory data [*Jackson and Faul*, 2010] show a nonlinear dependence of shear modulus on temperature, particularly within 150–200°C of the solidus, which we assume to be ~1350°C. To account for increasing anelastic effects with increasing temperature, we must relax the linear relationship between density and velocity at low velocities (Figure 3). Using the empirical relationship between shear modulus and temperature

for 1 mm diameter olivine crystals [*Jackson and Faul*, 2010] and a coefficient of thermal expansion of 3×10^{-5} per °C, we calculate that the last ~150–200°C before the solidus manifests as decrease in seismic velocity of ~3%.

To estimate the velocity that corresponds to the 1200°C isotherm, or the approximate temperature below which an elastic velocity-density relationship is valid, we note that the maximum velocity found by *Shen et al*. [2013a] at 120 km depth is 4.75 km/s and is observed in the Wyoming craton. Here the thermal boundary layer is ~200 km thick [e.g., *Schutt et al*., 2011]. If the geotherm is approximately linear, the expected temperature at 120 km depth is ~820°C (surface temperature 20°C). Again using the shear modulus data for 1 mm olivine [*Jackson and Faul*, 2010] and a coefficient of thermal expansion of 3.2×10^{-5} per °C, we find that this 380°C temperature contrast corresponds to a 5.5% velocity difference. The 1200°C isotherm therefore corresponds roughly to a velocity of 4.75/1.055 = 4.50 km/s. For wave speeds below that of the solidus, we expect most seismic variation to be due to the increased presence of melt. Because melt produces small changes in bulk density (between 0 and 4 kg/m^3 per 1% in situ melt fraction) [e.g., *Hammond and Humphreys*, 2000], we assume that density is constant for wave speeds more than 3% lower than 4.50 km/s (i.e., $<$4.37 km/s).

We assume that there is no variation with depth of our velocity to density relationship largely because of uncertainty in the depth variation of anelastic effects. Certainly the solidus occurs at increasingly lower velocities at greater depth, but the volume of material affected is small and has little effect on our calculations. If the solidus occurs at 2% lower velocity at 150 km than at the Moho, then we will underestimate density an average of up to 7 kg/m^3 in the mantle. Thus, by equation 2, errors introduced by the constant-solidus approximation might yield errors in our estimate of topography of up to 200 m.

We assume that mantle loads are fully coupled to the overlying crust and surface (although resultant topography is modulated by the flexural filter). The degree to which loads present in a deforming viscous medium affect surface topography depends on the viscosity structure of the medium and load wavelength [e.g., *Parsons and Daly*, 1983]. Nevertheless, the lateral resolution (~100 km) of dispersion curve inversions and long wavelength (200–300 km) of velocity anomalies reported by *Shen et al*. [2013a] are broad enough that we treat mantle loads as fully coupled to the surface. We then smooth these values by the estimated flexural response of the lithosphere. Following these assumptions, we calculate the mantle topography (Figure 4a).

3.2. Crust-Supported Topography

We assume that seismic wave speeds in the crust depend on some combination of composition and temperature. We convert *S* wave speeds to density within the crust using *Brocher*'s [2005] regression of density onto *S* wave speed and a correction for thermal variations based on estimates of temperature variations in the crust, discussed below.

The assumption of an isothermal crust would maximize estimates of crustal density variations, as the partial derivatives $\partial\rho/\partial v_{s(\text{temperature})}$ and $\partial\rho/\partial v_{s(\text{composition})}$ are different. Regressions of density onto velocity [*Brocher*, 2005; *Christensen*, 1996] show that near $v_s = 3.9$ km/s ($v_p = 6.7$ km/s and $\rho = 2900$ kg/m^3), $\partial\rho/\partial v_{s(\text{composition})} \approx$ 523 kg/m^3 per km/s, while $\partial\rho/\partial v_{s(\text{temperature})} = 249.2$ kg/m^3 per km/s. Here we assume a coefficient of thermal expansion of 2.5×10^{-5} °C^{-1}, a v_p/v_s of 1.78 that is insensitive to temperature, and a $\partial v_p/\partial T$ of -0.5 m/s per °C [*Christensen and Mooney*, 1995]; this calculation is discussed below. Because of this difference, and because we aim to quantify the tectonic significance of crustal temperature variation, we seek to separate the minor (-0.281 m/s °C^{-1}) velocity (and thus inferred density) variations due to temperature from those due to composition, and to do so we must estimate the mean temperature of the crust.

We use surface heat flow observations (from *Southern Methodist University Geothermal Database* [2012]; http://smu.edu/geothermal/georesou/DataRequest.asp, accessed on 11/15/2012) smoothed over a 100 km radius as a proxy for crustal temperature (Figure 4c). Obviously, such a data set places only some constraints on the overall thermal structure of the crust as hydrological effects, varying thermal conductivity, variable radioactive heat generation, and disequilibrium geotherms all will disrupt the relationship between surface heat flow and subsurface thermal structure. We follow *Hasterok and Chapman* [2007a] and avoid any attempt to correct for these issues, as observational constraints on all of these parameters are weak and spatially irregular.

We instead assume a simple linear geotherm through the crust and that this geotherm is accurately reflected in the heat flow. For example, if we assume a conductivity of 3 W/m°C, then a heat flow of 75 mW/m^2, such as

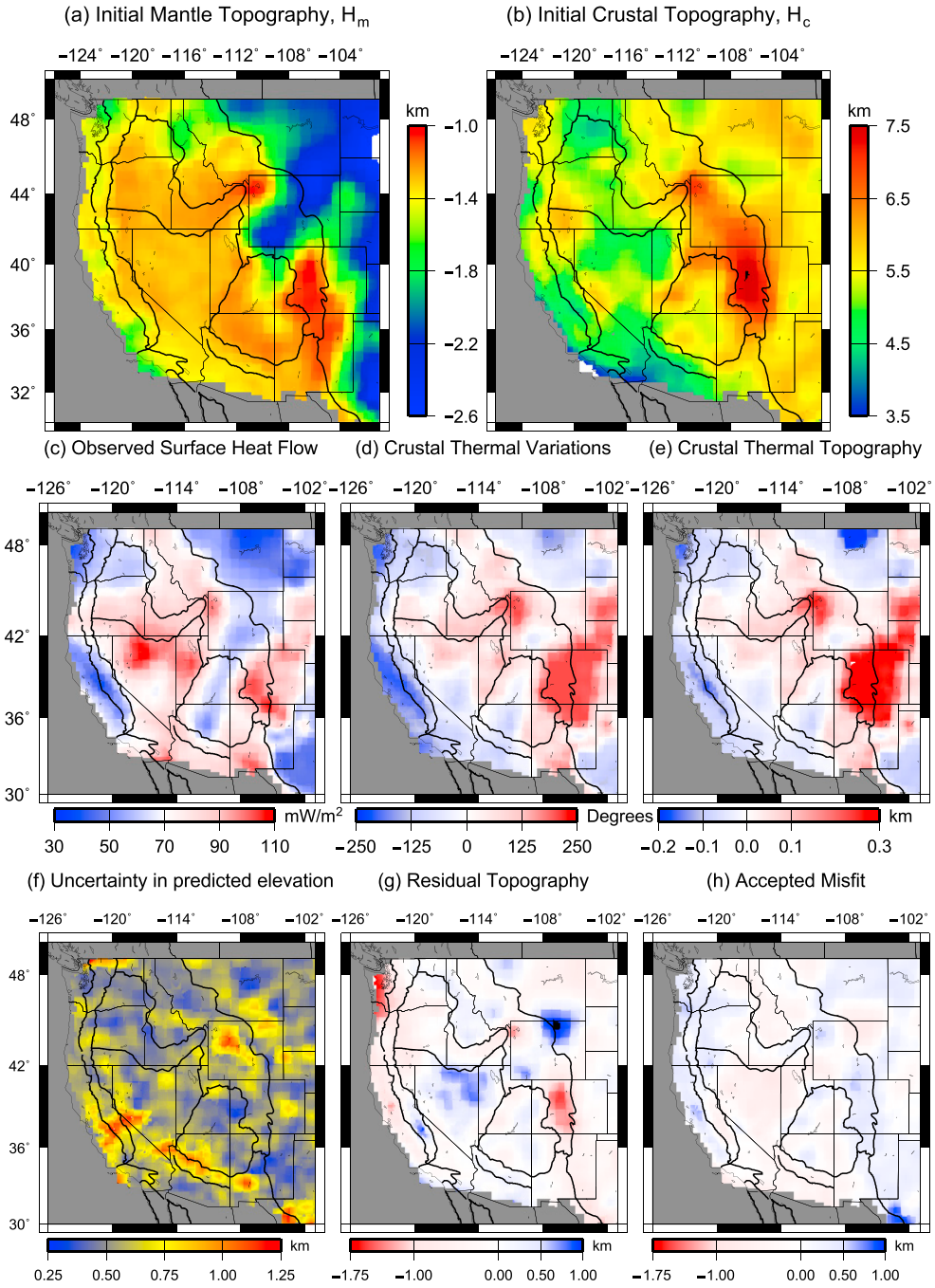

Figure 4. (a) Initial estimate of mantle topography. Note large, negative values in the Wyoming Craton and Great Plains, especially when compared to the relatively constant value in the southern Rockies, Colorado Plateau, and Basin and Range. (b) Initial estimate of crustal topography. Note large magnitude of support from the crust of the southern Rockies and Wyoming craton. (c) Observed surface heat flow from SMU Geothermal Database. (d) Color scale is chosen to reflect conversion into mean crustal temperature, which is described in the text. (Figure 4d) Estimated mean crustal temperature variations, based on heat flow. (e) Topography variations arising from estimated crustal thermal structure. Note ~500 m peak-to-trough amplitude. (f) A 2σ uncertainty in predicted elevation, derived from the envelope of acceptable velocity profiles. Mean 2σ uncertainty is 590 m. (g) Residual topography, H_r, as defined in equation 4. Negative values indicate an underestimate of density or existence of a positive downward basal normal force being exerted on the lithosphere that is not reflected in the seismic velocity. Positive values indicate upward basal normal force or density overestimate. (h) Accepted misfit between predicted and observed topography. All values are within uncertainties shown in Figure 4f. Color scale as in Figure 4g.

in the southern and central Basin and Range, corresponds to a crustal geotherm of ~25°C/km and a Moho (30–35 km) temperature of ~850°C. Since the maximum reasonable Moho temperature is that of convective asthenosphere, we limit the temperature to 1350°C. Also, for a region with a 200 km thick thermal boundary layer, a 50 km deep Moho would be no colder than 350°C, so we place this as the minimum temperature. This approximation neglects heat production in the upper crust, however. We explore the consequences of this simplification briefly below.

Our estimate of crustal density is thus derived from our inferred temperature variation and the observed shear wave speed:

$$\begin{aligned}\rho &= \rho_{\text{Brocher}}\left(v_s - \frac{\partial v}{\partial T}\Delta \text{T}\right) + \frac{\partial \rho}{\partial T}\Delta T \\ &= \rho_{\text{Brocher}}\left(v_s - \frac{v_s \partial v_p}{v_P\, \partial T}\Delta T\right) + (1 - \alpha \Delta T) \\ &= \rho_{\text{Brocher}}\left(v_s + 0.28\frac{m/s}{^\circ C}\Delta T\right) + \left(1 - 2.5{\cdot}10^{-5}(^\circ\text{C})^{-1}\Delta T\right)\end{aligned} \tag{3}$$

where $\rho_{\text{Brocher}}(v_s)$ is the combined regression of v_s on v_p and v_p on density of Brocher.

For example, the regression of density onto velocity suggests that a 0.1 km/s increase in velocity due to compositional variations corresponds to a ~52.3 kg/m^3 higher density. Alternatively, a temperature difference of −356°C would also increase velocity by ~0.1 km/s. This temperature difference corresponds to a density increase of only ~25 kg/m^3. The compositional regression thus overestimates the density of "cold" material by a factor of ~0.08 kg/m^3 °C^{-1}. Modest velocity variations due to temperature can lead to tectonically significant errors in predicted density (in a 40 km crust, the error above would produce ~400 m of topography), and ascribing all velocity heterogeneity to composition or to temperature will lead us to calculate inaccurate densities.

Assuming a linear geotherm in the crust will overestimate mean crustal temperatures. For example, a region of 75 mW/m^2 surface heat flow and 40 km thick crust—both typical of the western U.S.—would be predicted to have a Moho temperature of ~1020°C limit if radioactive heat production is ignored. If, instead, heat flow largely reflects radiogenic heat in the upper 10 km and reduced heat flow is ~40 mW/m^2—a low value for the western U.S. [*Blackwell*, 1983; *Saltus and Lachenbruch*, 1991]—the Moho temperature would be a more modest 670°C. The average temperatures of these crustal columns are 520°C and 390°C, respectively. The error introduced by this 130°C mismatch is, on average, ~10 kg/m^3. Following equation 2, we would underestimate H_c by 130 m. Thus, we will tend to underestimate H_c in areas with high radiogenic heat production. Nevertheless, since the variation in heat production within provinces is similar [*Morgan and Gosnold*, 1989] we expect that this effect mostly produces a relatively uniform underestimate in H_c near or under 100 m. The approximation of the thermal regime is thus likely adequate for our purpose owing both to the unknowns in the thermal structure and the relatively small contribution to topography from thermal variations within the crust, which, as we discuss below, has a total range of about 500 m (Figure 4e).

Taking these inferred temperature perturbations (Figure 4d) into account, we calculate crustal topography throughout the western U.S. (Figure 4b). We note that *S* wave speed variations caused by melt (7.9% decrease per 1% in situ melt fraction) produce far smaller changes in bulk density than composition or temperature (between 0 and 4 kg/m^3 per 1% in situ melt fraction) [*Hammond and Humphreys*, 2000]. This bias will cause H_c as calculated here to be too great in areas with crustal melts, a bias we consider in addressing areas of topographic misfit below.

4. Topography Uncertainties

The posterior distribution of wave speed structures from the Monte Carlo investigation of seismic models of *Shen et al*. [2013b] allows for a direct analysis of the uncertainty of our topographic calculations due to seismic velocity and crustal thickness uncertainties. Each individual velocity profile and crustal thickness is converted into a density profile, and the attendant crustal and mantle topographies are calculated. The resulting ~1000 estimates of H_c and H_m at each point define the seismic uncertainty in our results (Figure 4f).

We have quantified the uncertainty in our topography estimates and investigated its origins. We find that the variation in elements of the posterior distribution of v_s models overwhelms the uncertainties in converting

velocity to density. As illustrated in Figure 2, basing predictions of elevation on a single velocity profile not only may produce systematically biased results but also underestimates the uncertainty of the prediction, even if the uncertainty in density derived from velocity is considered. In fact, once the full posterior distribution of velocity models is analyzed, incorporation of such uncertainty yields no further variation in the predicted topography. Even if deviations from the presumed velocity-density relationship correlate over layers 10 km thick, uncertainties in H_c increase by less than 50 m. Vertical correlations would have to be crustal in scale, significantly greater than the ~5 km length suggested by investigations of the Ivrea Zone [e.g., *Goff et al*., 1994; *Levander and Holliger*, 1992; *Holliger and Levander*, 1992], to have an impact comparable to the uncertainty in velocity profiles. Thus, we do not include uncertainties in the velocity to density conversion in our uncertainty of H_c. Substantial and systematic deviations of a region from the assumed velocity-density relationship will produce equally systematic deviations of the calculated topography from that observed. We discuss such occurrences below.

A potential difficulty arises if large magnitude, long wavelength variations in radial anisotropy are present. We have assumed that the v_{SV} profiles used are sufficiently close to the mean shear wave speed of the crust and mantle for calculation of densities. However, the presence of variations in radial anisotropy would produce biases; we would be underestimating the Voigt average shear velocity by ~1.5% in areas where radial anisotropy was ~5%, in which case we would overpredict topography by about 800 m relative to isotropic sections if the anisotropy extended through the entire crust and mantle to ~150 km depth. Variations inferred by *Moschetti et al*. [2010] for the area west of 110°W suggest we might be underpredicting elevation in the Colorado Plateau and further underpredicting elevation in the Sierra Nevada by some few hundred meters. At a longer wavelength, the model of *Marone et al*. [2007] suggests that we could be overpredicting elevations in the southern Rockies by several hundred meters. Owing to the present low resolution of and variations among existing models of radial anisotropy, we do not explicitly correct for this effect.

Other limitations that could affect our results arise from the parameterization of the seismological model. Crustal low-velocity zones are prohibited, and sharp increases in wave speed are only permitted at the base of sediments and at the Moho. Since surface wave dispersion at a given frequency is sensitive to a wide depth range, low-velocity zones would, to first order, result in a broad region of lower wave speeds in the surface wave models. The topography calculations, however, are integrals through the crust and upper mantle. Thus, the fact that low-velocity zones are not allowed in the crust does not substantially affect our conclusions. Strong discontinuities at depth other than the Moho could result in material being assigned the wrong velocity to density function; this is presumably most likely in areas where "double Mohos" are present (e.g., southern Wyoming [*Karlstrom et al*., 2005]). The error here depends on whether the seismic inversion has selected the top or bottom Moho and the velocity of the material between the two Mohos. Take, for example, a 10 km thick underplate with a velocity of 4.3 km/s (v_p ~7.5 km/s). We would calculate a density of 3137 kg/m^3 and H_c of 197 m from this body (following equation 2). If the receiver functions show "Moho" above this body, however, we would calculate a density of 3185 kg/m^3 and an H_m of 47 m. The total error in topography is thus ~150 m.

5. Comparison to Topography and Adjustments to Densities

Where our combined crustal (Figure 4b) and mantle (Figure 4a) variations reproduce observed topography acceptably (to the limits shown in Figure 4f), lithospheric thermal and crustal compositional variations are sufficient to support the topography. Elsewhere, other factors presumably affect the velocity-density relationship or the surface elevation. The factors include the presence of crustal melt, compositional variations in the mantle, lithospheric mantle extending below the model, or normal stress derived from the convective regime of the asthenosphere (dynamic topography). To identify these areas more clearly, we calculate the residual topography, H_r, (Figure 4g) which represents the smoothed topography (Figure 1a) minus the topography calculated from our initial assumptions, ε_c.

$$H_r \equiv \varepsilon - \varepsilon_c = \varepsilon + H_0 - H_c - H_m \tag{4}$$

Thus, positive residual topography denotes a higher observed elevation than predicted by a given model. In light of the appreciable uncertainties (mean $2\sigma = 590$ m), we pay particular attention to regions where H_r exceeds our calculated uncertainty (Figure 5a).

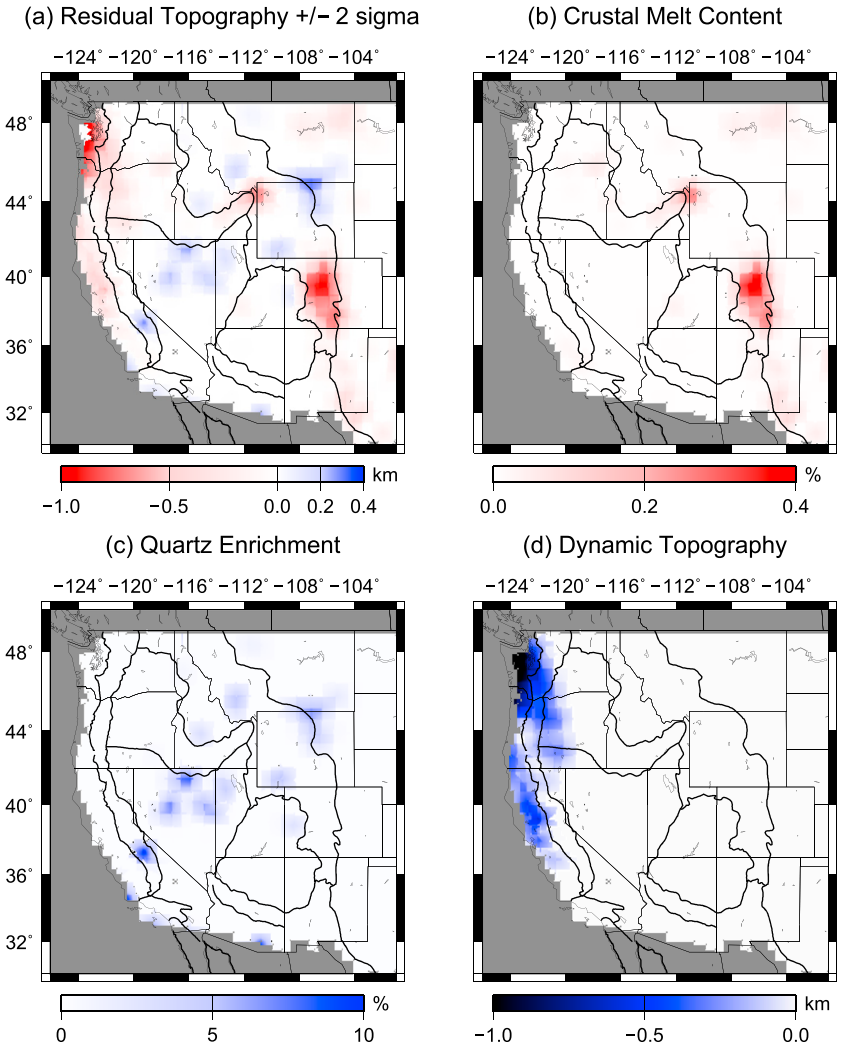

Figure 5. (a) Statistically significant residual, or H_r (Figure 4g) plus/minus uncertainty (Figure 4f). (b) Minimum amount of in situ melt, averaged through the crust that we propose contributes to H_r. (c) Minimum amount of quartz increase, averaged through the mantle lithosphere that we propose contributes to H_r. (d) Minimum amount of dynamic (downward) topography that we propose contributes to H_r. Approximately 30 MPa downward normal force would produce 1 km of surface depression.

As seen in Figure 5a, elevations in ~84% of the study area are matched within uncertainty by a combination of compositional and thermal variations in the crust and thermal variations in the mantle. In the Yellowstone region, Cascadian fore arc, and Southern Rocky Mountains, elevations are coherently predicted to be 0.5–1 km higher than observed. This discrepancy can be eliminated in one of two ways: imposing a downward normal stress of 15–30 MPa on the lithosphere (i.e., dynamic subsidence), or systematically increasing lithospheric density. Since we use Brocher's regressions of v_s onto v_p and v_p onto density, pervasive quartz-poor crust and its high v_p/v_s ratio would lead us to underestimate density for an observed seismic velocity. Alternatively, the presence of melt drastically reduces velocities but has a lesser effect on density and would thus cause us to underestimate density.

Near Yellowstone and in the southern Rockies, negative residual topography coincides with heat flow in excess of 100 mW/m^2 (Figure 4c), high seismic attenuation in the crust [e.g., *Phillips and Stead*, 2008], somewhat low crustal v_p/v_s ratio [*Lowry and Perez-Gussinye*, 2011], and inferred near-solidus or suprasolidus mantle temperatures (see Figure 4a). For these reasons, we favor the explanation that partial melt is present in the crust in these areas (Figure 5b), though we recognize that presence of melts in the mantle at subsolidus temperatures would also produce an error in calculated density. In a crustal column with original *S* velocity of

3.15 km/s that contains an average 1% melt, wave speeds decrease by 0.25 km/s (following *Hammond and Humphreys* [2000]). We would misinterpret such a decrease as a 135 kg/m^3 (~5%) density decrease and, when integrating through a 40 km crustal column, would overestimate crustal topography by 1.7 km. Thus, ~0.3% in situ partial melt throughout the ~40 km crust near Yellowstone would account for ~0.6 km residual topography, as would 3% in a 4 km zone; we cannot discriminate between distributed and concentrated crustal melt especially as the shear wave structures we use prohibit crustal low velocity zones. A similar average amount of melt would resolve the discrepancy in the southern Rockies, though this could be lessened if radial anisotropy is indeed stronger in this area.

Conversely, −0.5 to −1 km residual topography in the Cascadian fore arc coincides with low heat flow. Geologically, the presence of substantial amounts of serpentine, with its unusual wave speed to density relationship, might be expected to contribute to this error. Although serpentinization lowers v_s substantially, using the nonlinear regressions of *Brocher* [2005] of v_s to v_p and v_p to density produces a misfit of only 111 kg/m^3 (~4%). A 10 km layer that is 50% serpentine increases estimated topography by only 175 m. Thus, the ~30 km crust would have to be nearly entirely serpentinite to account for the topographic residual. Instead, we propose that the fore arc is depressed by downward basal normal stresses of ~15–30 MPa exerted on the lithosphere by subduction zone processes (Figure 5d).

Elevations in the southern Sierra Nevada and northern Basin and Range (Figure 5a) and to a lesser extent Wyoming and the Idaho batholith (Figure 4g) are higher than expected by as much as 500 m. Overestimating density by 40 kg/m^3 (~1.4%) throughout a 40 km crust would account for this discrepancy. All of the regions in question (Figure 5c) coincide with low v_p/v_s estimated from receiver functions that *Lowry and Perez-Gussinye* [2011] interpret as reflecting a high-quartz content. Indeed, in the Sierra Nevada, the crust is thought to comprise only the upper, felsic portion of a Mesozoic-Cretaceous batholith [*Fliedner et al*., 2000; *Ducea and Saleeby*, 1998; *Levandowski et al*., 2013b].

Particularly felsic crust and its attendant low v_p/v_s would lead us to calculate systematically high densities, since we use Brocher's regressions of v_s onto v_p and v_p onto density. To estimate the mean amount of quartz increase necessary to reconcile seismic velocities and topography, we compare the observed and predicted densities of pure quartzite [*Christensen*, 1996], assuming that the polynomial regression [*Brocher*, 2005] is appropriate for average continental crust of ~60% SiO_2 containing ~10% quartz. The density estimated from our application of Brocher's regressions for a v_s of 4.035 km/s (200 MPa quartzite) is 2975 kg/m^3, but the density of quartzite is only 2652 kg/m^3. Thus, an increase in the modal abundance of quartz of ~90% corresponds to a 325 kg/m^3 (~11.6%) bias in density. Thus, a 500 m elevation error can be explained by an increase in the modal abundance of quartz of ~11% throughout the crust.

Overestimated topography could also be attributed to variations in mantle chemistry. Increasing Mg# (Mg#=MgO/[MgO+FeO]) of olivine in mantle lithosphere both increases velocity (~0.3% per 0.01 increase in Mg#) and decreases density (~8.5 kg/m^3 or ~0.02% per unit increase in olivine Mg#) [*Schutt and Lesher*, 2010]. Thus, an increase of ~0.01 in Mg# can resolve the apparent discrepancy between seismic velocity and elevation. Because we might suspect significant iron depletion in the Wyoming craton and we observe large magnitude, long wavelength, positive residual topography there (Figure 5a), we discuss this possibility below.

We desire to account for the effects of melt and varying quartz content in order to more clearly examine the contributions of crust and mantle to topography; thus, we modify the density structures calculated assuming thermal variations throughout the lithosphere and compositional variations in the crust (topography of which is shown in Figure 4). These modifications affect ~12% of the study area. To recover topography, a mean crustal density adjustment of $\Delta\rho$:

$$\Delta\rho = -H_r\left(\frac{\rho_a}{z_c}\right) \tag{5}$$

is necessary, with residual topography, H_r, as defined in equation 4, asthenosphere density $\rho_a = 3200$ kg/m^3, and crustal thickness z_c. Adding this term to the previously derived structures yields an adjusted density structure and final estimate of crustal compositional topography (Figure 6d).

These adjustments are relatively small, especially when compared to the ~60 kg/m^3 (~2.1%) standard errors associated with a linear velocity-density scaling [*Christensen and Mooney*, 1995]. Where applied, the mean

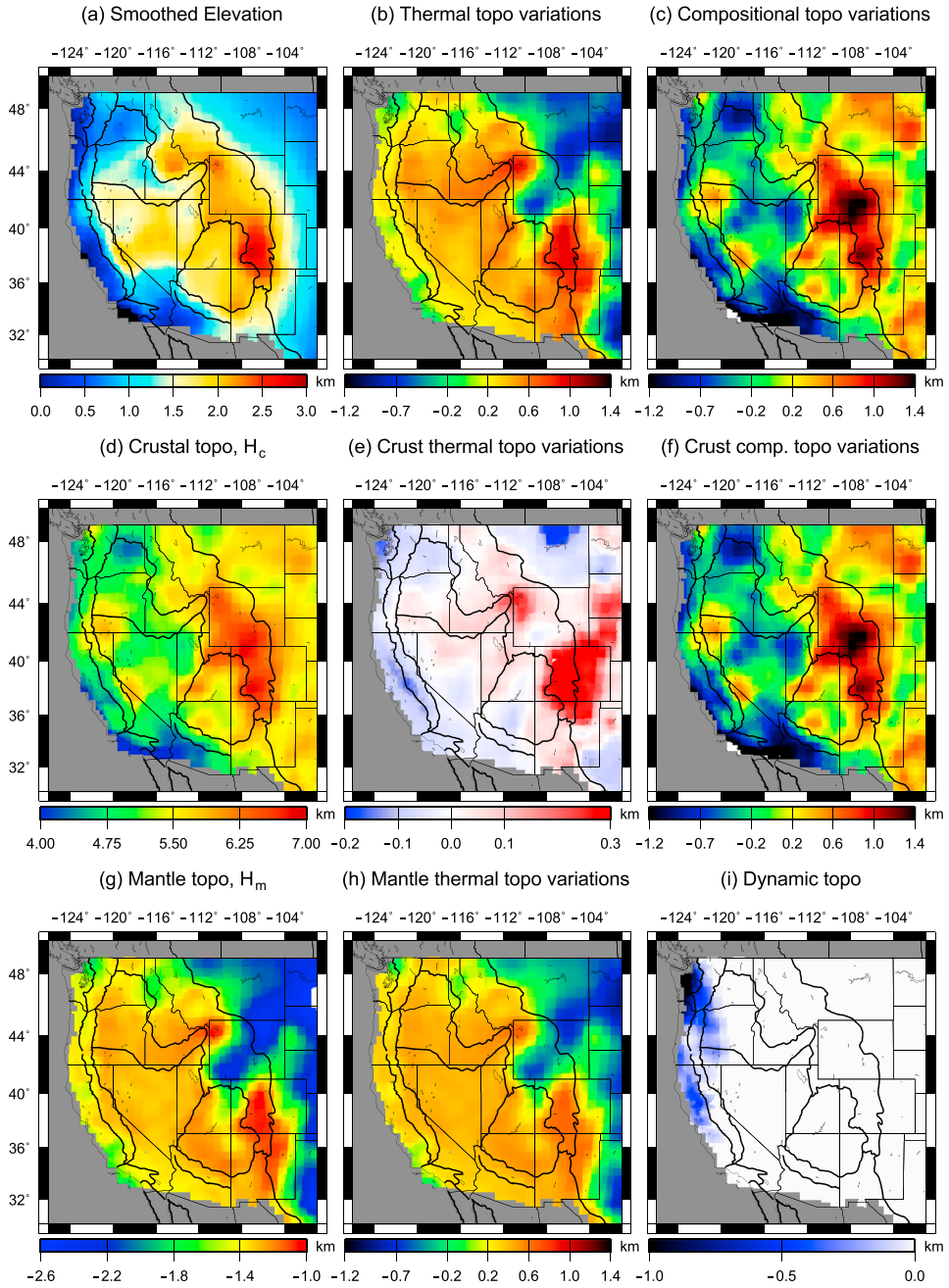

Figure 6. (a–i) Components of topography. Same scale is used in Figures 6b, 6c, 6f, and 6h. (Figure 6a) Flexurally smoothed topography of the western U.S. Same as Figure 1a. (Figure 6b) Topographic variations due to thermal variations (i.e., $H_{c\ \mathrm{thermal}} + H_{m\ \mathrm{thermal}}$ with the mean removed to facilitate comparison). Note consistent values in Basin and Range, Snake River Plain, and Southern Rockies. Note also low values in Wyoming craton and Great Plains. (Figure 6c) Topographic variations due to compositional variations (i.e. $H_{c\ \mathrm{comp}} + H_{m\ \mathrm{comp}}$ with the mean removed to facilitate comparison). Note very high values in the Wyoming craton, high values in the southern Rockies and Colorado Plateau, and low values in the Basin and Range. (Figure 6d) Final estimate of crustal topography, representing initial estimate (Figure 4b), corrected for the effect of proposed melt and quartz content (Figures 5b and 5c). (Figure 6e) Same as Figure 4e. Topography variations arising from estimated crustal thermal structure. (Figure 6f) Crustal compositional topography, representing total crustal topography (Figure 8c) corrected for estimated thermal topography of the crust (Figures 4e and 7d). Values are presented with the mean removed for more ready comparison. Note high values in the Great Plains, Rockies, and Colorado Plateau (0.5 to 2 km) as compared to the Snake River Plain and Basin and Range (<0 km). (Figure 6g) Mantle topography, same as Figure 4b. (Figure 6h) Mantle thermal topography, same as Figure 7g, but with the mean removed and then plotted on the same scale as Figures 7b, 7c, and 7f. Note large contrast between the Wyoming craton and Great Plains (values −0.5 to −1.4 km) and the Southern Rockies, Snake River Plain, Colorado Plateau, and Basin and Range (nearly constant values of 0.6 to 0.85 km). (Figure 6i) Dynamic topography as in Figure 5d.

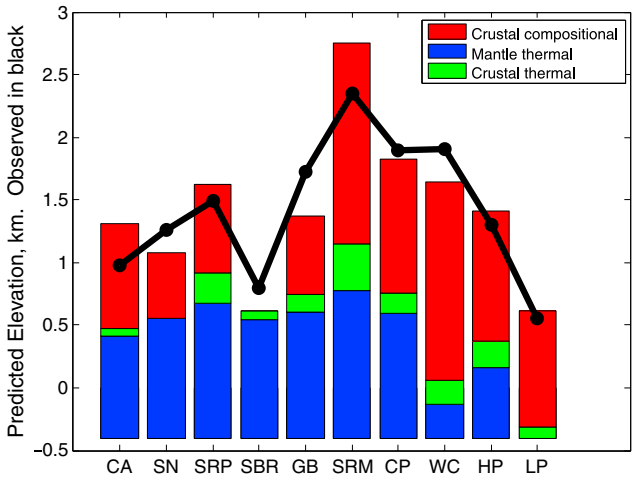

Figure 7. Bar graph of the average components of topography by province (CA = Cascades, SN = Sierra Nevada, SRP = Snake River Plain, SBR = southern Basin and Range, GB = Great Basin/northern Basin and Range, SRM = Southern Rocky Mountains, WC = Wyoming, HP = High Plains—smoothed elevations above 1 km, LP = Low Plains—smoothed elevations below 1 km). The minimum of each component is set to zero to better examine variations. Note similar mantle thermal topography from the Cascades through the Rockies and the strong difference between these regions and Wyoming/Plains. Other topography is mostly crustal in origin and dominated by compositional variation. Average smoothed elevation is shown in black for comparison. Misfits between predicted and observed are within uncertainty (see Figure 4h).

increase in crustal density due to melt is 23.5 kg/m^3 (~0.8%), and the mean decrease in crustal density from quartz content is −17.7 kg/m^3 (−0.6%).

6. Results

With the adjusted density estimates as described above, we examine three characteristics: the decomposed topography, predicted gravity, and gravitational potential energy. The values calculated for these and other parameters are presented in the electronic supplement.

6.1. Topography

We have determined a set of mantle and crustal densities that accord with both seismic velocity and topography. Nearly all of the variation in topography (Figures 1a and 6a) across the western U.S. arises from compositional (Figures 6c and 6f) and thermal (Figures 6b, 6e, and 6h) variations expressed in wave speed variations. Elsewhere (Figure 5a), in areas where crustal melt or highly felsic crust [*Lowry and Perez-Gussinye*, 2011] are likely, the relationship between velocity and density must be slightly adjusted. Taking these small adjustments (equation 5) into account, we can further separate modern topography into thermal and compositional components (Figures 6 and 7).

In addition to dynamic topography (Figures 5d and 6i), there are exactly four isostatic components of topography: mantle thermal (Figure 6h), mantle compositional, crustal thermal (Figure 6e), and crustal compositional (Figure 6f; where both thickness (Figure 1b) and chemistry (Figure 8) are considered).

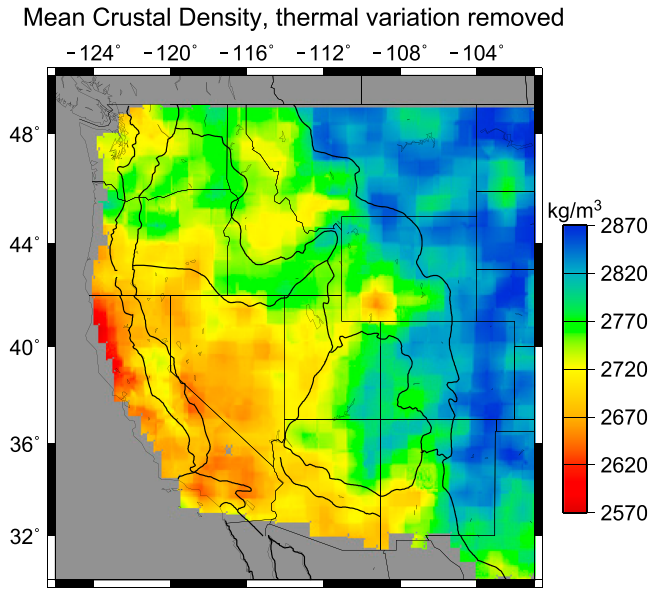

Figure 8. Crustal density from seismic velocities after the estimated thermal variations (Figure 4d) are removed. Note contrast between Wyoming and Southern Rockies.

We have assumed that all density and velocity variations in the mantle are thermal in origin and have found no locations violating this assumption beyond uncertainty. We acknowledge two shortcomings of this assumption, however. First, the seismic velocity models only extend to 150 km. The high velocity, presumably lithospheric material below this depth that is seen in other velocity models would provide negative buoyancy if included in our analysis. For example, in the Wyoming craton, where our current analysis suggests a need for a small amount (~200 m) of additional buoyant support (Figure 5a), a ~2% velocity anomaly extends to ~250 km depth [e.g., *Schmandt and Humphreys*, 2010]. This 14 kg/m^3 thermal density anomaly could plausibly be countered by Mg# increase of

~1.6%. This depletion would supply ~400 m of buoyant height if present over 100 km thickness. The second shortcoming of our analysis with regard to the mantle (and crustal) chemistry is the combination of >500 m analytical uncertainty (Figure 4f) with systematic patterns of residuals (Figures 4g, 4h, 5a, and 7). Our technique is insensitive to province-scale deviations from mantle isochemistry (or similar scale, systematic variations in crustal chemistry) that produce up to ~500 m of topography. To illustrate the magnitude of mantle depletion that our current analysis may be failing to recognize, we return to the Wyoming craton. The initial misfit to topography (Figure 4g) is ~700 m. If due to the upper 100 km of the lithospheric mantle (~50–150 km), this misfit would correspond to an increase in Mg# of ~2.6. Combining this plausible depletion of the upper 100 km of the lithosphere with the plausible depletion from 150 to 250 km, mantle composition could account for ~1.1 km of buoyant height in the Wyoming craton.

In the crust, we have estimated a mean temperature, and thus (following equation 2) the effect of thermal expansion and contraction, Hc_{thermal}, is (Figure 6e):

$$Hc_{\text{thermal}} = z_c \rho_0 \alpha \Delta T / \rho_a \tag{6}$$

where z_c is crustal thickness, ρ_0 is the crustal density, α is the coefficient of thermal expansion ($2.5 \times 10^{-5} ^{\circ}\text{C}^{-1}$), and ΔT is derived from heat flow. Then, the crustal compositional topography (Figure 6f) is given as follows:

$$Hc_{\text{comp}} = H_c - Hc_{\text{thermal}} \tag{7}$$

Examining the different components of topographic support (Figures 6 and 7), it is clear that differences in elevation among the southern Basin and Range, the Great Basin, the Colorado Plateau, and the southern Rockies are mostly to be found in differing crustal characteristics (Figures 6d–6f) rather than heterogeneity in the mantle.

Wyoming, the one Cordilleran province lacking warm mantle, is higher than the plains because of higher crustal compositional topography (Figure 6f). We note also that since our density models recover topography and gravity (presented below) in the Wyoming craton reasonably well, the high velocities observed below 150 km [e.g., *Burdick et al*., 2008] either represent cold but iron-poor isopycnic material or require somewhat lower densities in the mantle above 150 km.

Mantle topography accounts for the eastward descent from 2.5 km elevations in the Rockies to less than 1 km in the Great Plains.

6.2. Comparison to Gravity

Our adjusted density structure can be tested by calculating gravity anomalies from it and comparing these to the observed Bouguer anomaly (an alternative approach, as followed by *Mooney and Kaban* [2010], uses gravity as a primary observable and deduces density variations from gravity). We note first, however, that the predicted gravity field at a given station is strongly dependent on the shallow structure beneath that station. The top few kilometers is poorly constrained seismically because of limited sampling at higher frequencies. Furthermore, the use of receiver functions in determining acceptable seismic models can impart a local bias; the structure beneath a station may not be representative of the surrounding ~70 km.

We do not have a direct way to track the uncertainty of gravity, because we make use the entire posterior distribution of 1-D velocity profiles, and gravity is sensitive to density in 3-D. Instead, we may estimate the uncertainty from the mean topographic uncertainty, ~600 m. This uncertainty corresponds with an uncertainty of 48 kg/m^3 through 40 km crust. Such an error would produce 47 mGal of gravity misfit. Alternatively, we can calculate the uncertainty at each station that results from the seismological uncertainty in its 1-D posterior distribution. These uncertainties range from ±10 to ±40 mGal (2σ). Uncertainties for our 3-D gravity will be greater to the degree that errors in seismic wave speeds are laterally correlated. Thus, in considering gravity residuals, we bear in mind these crude estimates of uncertainty.

We estimate the Bouguer anomaly from our preferred 3-D density, including adjustments for inferred crustal melt and quartz enrichment; details of this calculation are presented in the Appendix A. The 3-D gravity prediction (Figure 9a) recovers the overall Bouguer anomaly variations of the western U.S. (Figure 9b) to within a few tens of milligals (Figure 9c). The misfit has mean magnitude of 25 mGal, well below our crude estimate of uncertainty. The misfit is less than 60 mGal in 95% of the study area and below 30 mGal in 75%. Nevertheless, there are systematic provincial residuals that suggest coherent errors in estimated density. A regional misfit of 30 mGal corresponds to a consistent density error of 20 kg/m^3 throughout a 40 km crust,

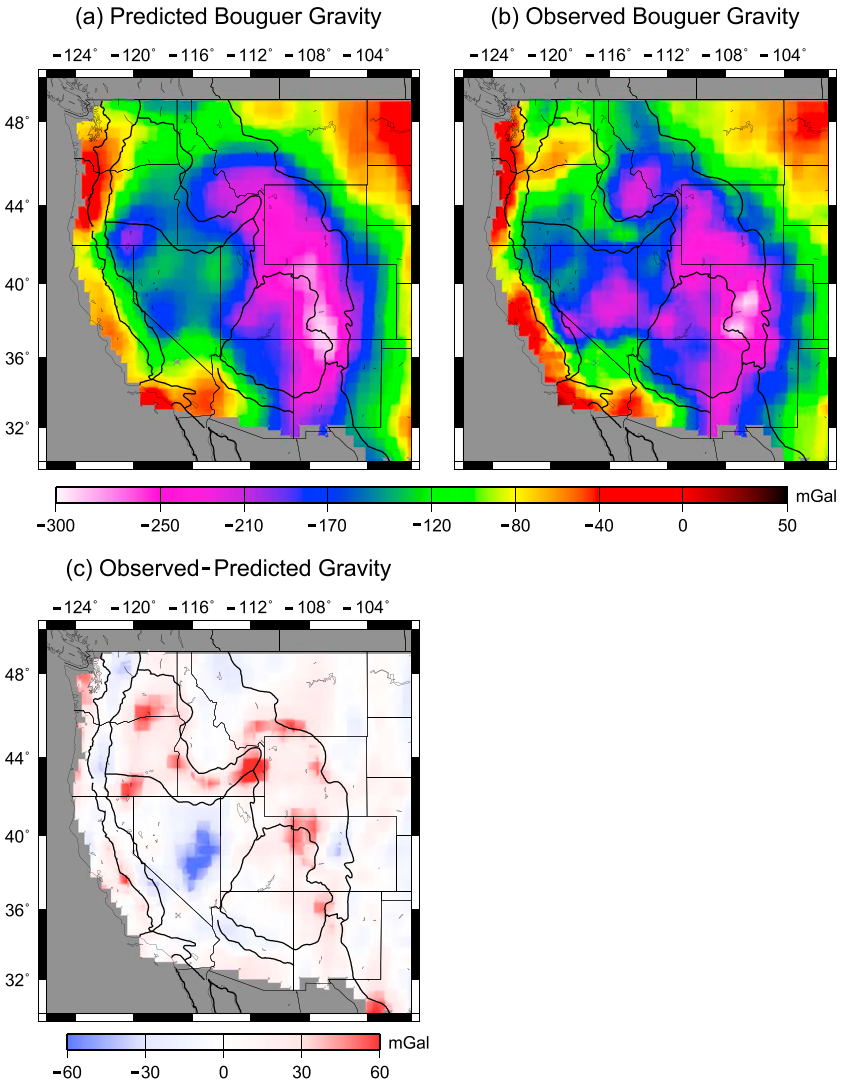

Figure 9. (a) Predicted Bouguer gravity field from our proposed density model. A correction (described in the text) is applied to mimic the effect of the Juan de Fuca slab. (b) Observed Bouguer gravity field. (c) Observed-predicted gravity field. Ninety percent of the study area is matched within 40 mGal.

though this density error would only produce 250 m of topography. We do not investigate the origins of low magnitude but regionally coherent misfit in gravity (Figure 9c) and/or topography (Figures 4g, 4h, 5a, and 7), but these could be due (among many other things) to regional differences in mantle chemistry (as discussed above), crustal geotherm, anisotropy, or crustal mineralogy.

6.3. Gravitational Potential Energy

Lateral variations in pressure that arise from topography and density differences generate stresses within the lithosphere, with areas of high integrated pressure (or GPE) exerting compressive stress on adjacent regions of lower GPE. From distributions of density, we can calculate the GPE available to modulate the stress field imposed by basal and edge forces:

$$\mathrm{GPE} = \int_0^{150+E} \rho(z) g z \, dz \tag{8}$$

where z is positive upward from the model base (in this case 150 km depth, such that mean sea level is at $z = 150$ km), and E is the surface elevation. We compare GPE to that of an asthenospheric column [*Jones et al.*, 1996] of density 3200 kg/m^3 that extends from 150 km to 2.4 km depth (order 10^{14} N/m). This column

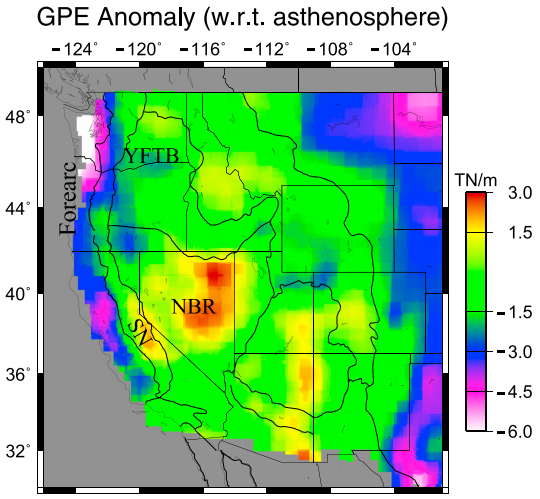

Figure 10. Gravitational potential energy (GPE) variations predicted from our preferred density model. Note positive GPE anomalies in the extending northern Basin and Range (NBR) and eastern front of the Sierra Nevada (SN). Also, note negative GPE along the western margin of North America, especially in the Cascades fore arc, with an arm of negative GPE extending eastward at the latitude of the Yakima fold and thrust belt (YFTB).

is calculated to be in isostatic equilibrium with a mid-ocean ridge [*Lachenbruch and Morgan*, 1990]. Such a column of asthenosphere should be free of deviatoric stresses, making it a useful reference state. High potential energy (positive anomaly, ΔGPE, relative to an asthenospheric column) increases horizontal deviatoric extensional stresses while negative ΔGPE favors contractional deformation. Lateral variations in ΔGPE are of the order 10^{12} N/m (Figure 10), and uncertainties are of the order 10^{11} N/m, up to 10^{12} N/m.

The mean deviatoric stress acting between two idealized columns is the difference in GPE divided by the column, or lithospheric, thickness [e.g., *Sonder and Jones*, 1999]. To illustrate, for two adjacent regions of 200 km thick lithosphere with a GPE contrast of 2×10^{12} N/m, the mean deviatoric stress exerted is 10 MPa. The magnitudes of these stresses are used by geodynamicists to calculate the magnitude of plate boundary stresses in the continental interior and to estimate the bulk viscosity of the lithosphere in thin viscous sheet models [e.g., *Flesch et al*., 2007]. For example, a 10 MPa stress in lithosphere with a bulk viscosity of 10^{23} Pa s would generate a strain rate of 10^{-16}/s, similar to values in the Idaho Batholith [e.g., *Payne et al*., 2013].

Positive ΔGPE is most prominent in the Sierra Nevada and the northern Basin and Range. The eastern front of the Sierra is, in fact, a locus of modern extension [e.g., *Unruh and Hauksson*, 2009] and the northern Basin and Range has been previously suspected to be a region of highly positive GPE [*Humphreys and Coblentz*, 2007; *Jones et al*., 1996]. The large-scale negative ΔGPE along the western margin of North America may be the result of surface depression due to subduction-related dynamic pressures (especially north of the Mendocino Triple Junction). A limb of negative ΔGPE projects eastward from the Cascade margin at ~46°N. This anomaly coincides with the Yakima fold and thrust belt, a zone of Quaternary deformation that may be connected to compressional strain along the Cascade margin [*Blakely et al*., 2011]. We propose that body forces modulate edge and basal stresses to create this pattern of contractional deformation.

7. Discussion

7.1. Topography and Earlier Studies

The explanation of western U.S. topography presented here differs from that inferred in earlier work; we consider here the origins of those differences and the implications for the validity of our results. *Jones et al*. [1996] did not use any seismological information for the mantle and instead inferred variations in H_m by assuming isostatic compensation in the asthenosphere. Values of H_c were mainly derived from *P* wave refraction profiles using the *Christensen and Mooney* [1995] wave speed-density regressions with no correction for lateral thermal variations. Most of our values of H_c are quite similar where seismic models were available to Jones et al.; the most notable differences are significantly lower H_c values (Figure 6d) in the California Central Valley and Colorado High Plains (which are due at least in part to the thermal effects on crustal wave speed-density relations that Jones et al. ignored) and somewhat lower values in the northern Basin and Range. We only find ~350 m variation in support from the mantle within the Cordillera outside Wyoming (Figure 6f), about one quarter that of *Jones et al*. [1996]. The differences mainly reflect the explicit inclusion of mantle wave speed anomalies here and suggest that most of the topography Jones et al. attributed to mantle density variations is caused by other effects.

Hasterok and Chapman [2007b] focused on a more complex thermal analysis of North America but overall used nearly identical assumptions as Jones et al. in correcting for varying compositional H_c in trying to

reproduce topography across the region. We limit the use of surface heat flow to estimate crustal temperatures but *Hasterok and Chapman* [2007b] extended its use into the mantle. Although we share an assumption of a thermal origin for mantle density anomalies, we rely on seismic wave speeds to estimate mantle temperatures and thus density. Furthermore, we adjust observed wave speeds to account for thermal variations before interpreting chemical variations in the crust. They estimated, as we do (compare their Figure 4c with our Figure 6b), that thermal variations account for ~3 km of relief. The differences between surface heat flow and seismic wave speeds at depth suggests that much of the scatter *Hasterok and Chapman* [2007b] found can be attributed to nonsteady state thermal structure within the lithosphere. Unlike an extrapolation of surface observations into the mantle, our approach permits different thermal structures in the crust and mantle, implicitly allowing nonsteady state geotherms, which are reflected by seemingly inconsistent crustal (Figure 6d) and mantle (Figure 6g) thermal topography as in the Sierra Nevada and Colorado Plateau.

Our estimates of crustal compositional topography (Figure 6c) variations are generally of the same polarity but of different magnitude from *Hasterok and Chapman* [2007a]. Specifically, we tend to calculate much greater variations of crustal buoyancy within the Cordillera. For example, comparing the northern and southern Basin and Range, we propose that nearly all of the ~1 km of relief is compositional in origin, as are differences between these provinces and the southern Rockies (Figure 6c). In each case, *Hasterok and Chapman* [2007b] ascribe this relief to thermal variations.

Lowry et al. [2000] inferred from an analysis considering gravity and some seismic refraction models that about 2 km of topographic variation was caused by dynamic stresses applied to the lithosphere. Although our crustal buoyancy estimates are fairly close to theirs (compare our Figure 6d and their Plate 3b), we have a very different appraisal of the topography due to thermal effects in the mantle largely because we are interpreting seismic models in the mantle, but they projected surface heat flow measurements into the mantle. This disparity suggests that the lithosphere in the region is either not in a conductive steady state or has large deviations in conductivity or heat production from values presumed by Lowry et al., and this difference is why we do not infer the significant dynamical component to topography that they reported, at least away from the subduction zone.

7.2. Examples of Application to Province-Scale Tectonics

One can interrogate this subcontinental-scale model of the sources of topography to examine province-scale tectonics in a regional context. The comparison of two provinces, for example, allows for an explanation of modern relief; as an example, we explore the topographic disparity of the southern and northern Basin and Range (Figures 1a and 6a). Alternatively, with a constraint on paleoelevation and a knowledge the modern topographic components, one can examine the changes that may be responsible for surface uplift or subsidence; we do so for the Colorado Plateau.

The ~800 m of relief between the southern and northern Basin and Range has been variously attributed to plume-derived dynamic topography [*Saltus and Thompson*, 1995], variations in mantle lithospheric thickness [*Jones et al*., 1996] and/or chemistry [*Schulte-Pelkum et al*., 2011] and variations in crustal density [*Eaton et al*., 1978]. Examining Figures 6–8, we conclude that relief is generated by crustal compositional variation, not by mantle variations. Furthermore, this elevation difference is due not to crustal chemistry; mean thermally corrected densities (Figure 8) are 2726 kg/m^3 in the southern and 2716 kg/m^3 in the northern Basin and Range, which contributes ~100 m of relief. Instead topography arises from a crustal thickness difference of 4.5 km (Figure 1b), which accounts for 700 m of relief. Note that this interpretation is at odds with earlier estimates based on refraction studies [e.g., *Catchings and Mooney*, 1991] that showed a ~30 km crustal thickness throughout the Basin and Range. The receiver functions used here and other continent-scale receiver function studies [e.g., *Gilbert*, 2012] allow for a more uniform sampling of crustal thickness whereas the sparse available seismic refraction lines may preferentially sample anomalously thin or thick crust in a given region.

The Colorado Plateau has risen ~2 km since the Cretaceous, and this uplift has been attributed to a variety of processes, including (1) warming of the uppermost mantle either conductively [*Roy et al*., 2009] or by removal of the lower lithosphere recently [*Levander et al*., 2011] or during the Laramide [*Spencer*, 1996], (2) dynamic support from the mantle convective regime [*Moucha et al*., 2008], or (3) crustal thickening due to lower crustal flow [*McQuarrie and Chase*, 2000] or a lower crustal phase change [*Morgan*, 2003; *Jones et al*., 2011]. We find that the mantle thermal topography (compare Colorado Plateau and Great Plains in Figures 6g, 6h, and 7)

and the crustal chemistry (compare Colorado Plateau to Plains and southern Rockies in Figure 8) are responsible for the modern elevation, and modern topography does not require dynamic support (Figure 5d). The 40 kg/m^3 difference in crustal chemical density between the Plains and Colorado Plateau that we estimate lends ~500 m of relative support to the latter. Hydration of lower crust, as recorded in xenoliths [e.g., *Butcher*, 2013] is one possible means of changing crustal density since the Cretaceous. The remaining 1.5 km of uplift is suspiciously similar to the difference in mantle thermal topography between the Colorado Plateau and the lower part of the Great Plains (Figures 6g and 6h). If the continental interior serves as an estimate for the pre-Cretaceous Colorado Plateau [*Spencer*, 1996], then a change in the mantle thermal structure largely explains the change in topography. The magnitude of this inferred change suggests that mechanical replacement of the lower thermal boundary layer is more likely than conductive heating. For a ~90 km thick lithosphere [e.g., *Levander and Miller*, 2012], the mean lithospheric temperature would have to change by 520°C (and thus the base of the lithosphere by 1040 °C, even in the end-member case of a linear geotherm) to produce 1.5 km of uplift. Alternatively, removal of ~75 km of thermally equilibrated mantle lithosphere (i.e., with a linear geotherm) could produce 1.5 km of uplift [*Levandowski et al*., 2013a] over 70 Ma. A more detailed investigation of this process is deferred to another manuscript [W.B. Levandowski et al., Cenozoic uplift of the Colorado Plateau by lithospheric removal and crustal hydration: Insight from seismically-derived density models, Geology, manuscript in preparation].

7.3. Implications for Dynamic Topography

Previous workers have invoked dynamic topography, or basal normal stresses exerted by the convective regime of the asthenosphere, to explain elevations of the Colorado Plateau [*Moucha et al*., 2008; *Liu and Gurnis*, 2010], the southern Rockies [*Karlstrom et al*., 2012], or Yellowstone [e.g., *Pysklywec and Mitrovica*, 1997] although some of these studies include erosion of mantle lithosphere with the effects of basal normal stresses. Nevertheless, we present densities that recover modern elevations reasonably well, and since the gravity misfit (Figure 9c) is within expectations of our topographic uncertainties, we largely reject the role of dynamic pressures in supporting topographic variations in the Cordillera, except east of the vicinity of the Cascadia subduction zone (Figure 5d).

To illustrate, consider a region at sea level with isopycnic mantle lithosphere (i.e., $H_m = 0$) and 40 km thick crust of uniform density. If in isostatic equilibrium (i.e., $H_c = 2.4$ km), the crust must be 3008 kg/m^3. If a ~1 km of dynamic topography (basal normal force of ~30 MPa) is being generated by asthenospheric convection (i.e., $H_c = 1.4$ km), then crustal density is 3088 kg/m^3. The difference in the gravity signal from these two crustal columns is ~135 mGal in the infinite slab limit and 118 mGal if active over 300 km wavelength. Thus, given the absence of large magnitude, province-scale gravity residuals, we argue that the density structure that we estimate, and not dynamic topography, is responsible for the modern elevation of the western U.S.

7.4. GPE and Earlier Studies

Previous attempts to estimate GPE have necessarily relied upon the filtered geoid or interpolations of seismic models. With the availability of more uniform seismic coverage, however, we have been able to improve upon the limitations of former by including long-wavelength variations due to shallow (<150 km) structure and upon the latter by utilizing a near-uniform model coverage and uniform seismic data processing methods.

The locations of relative GPE anomalies vary substantially in earlier studies. In a study of similar spatial dimensions to ours, *Flesch et al*. [2007] estimate a GPE high in the southern Rocky Mountains and a general gradient downward toward the Pacific margin. Using the geoid somewhat differently, *Humphreys and Coblentz* [2007] suggested that the northern Basin and Range broadly, and northeastern Nevada specifically, was a region of high GPE and that the Rockies were nearly without GPE-derived deviatoric stresses. *Jones et al*. [1996] also found high GPE in northeastern Nevada, when using seismic velocities instead of the geoid. But unlike later work, they also found high GPE in the Sierra Nevada, low GPE on the western margin, and variable GPE in the southern Rockies. Our work, perhaps not surprisingly, more closely resembles this previous effort that uses seismic velocity than those using geoid. We find GPE highs in NE Nevada and the Sierra Nevada and a coherent, consistent GPE low along the western margin of the continent (Figure 10).

The magnitudes of GPE anomalies that we calculate are comparable to previous estimates [*Jones et al*., 1996; *Flesch et al*., 2007; *Humphreys and Coblentz*, 2007]. Ranges have been estimated at 4.5 TN/m, 9 TN/m, and 4.5 TN/m, respective to the citations above. Our estimated range is ~7 TN/m (with the exception of the unreliable edges of our model).

Although the implications of our new GPE estimates require a more complete analysis, certain effects can be illustrated by simple comparison with published work. In general, approaches to modeling lithospheric deformation tend to combine the stress field from a particular GPE distribution with that derived from boundary and basal stresses with the goal of matching some observable, typically the magnitude and/or orientation of the stress, strain rate or velocity field [e.g., *Flesch et al*., 2000, 2007; *Humphreys and Coblentz*, 2007]; the total effect of a difference in GPE distribution will depend on how this influences the derived boundary stresses, which in turn relates to the relative importance of boundary and internal stresses in driving deformation. If the differences do not much alter the estimated boundary stresses, then differences will be accommodated by changes in effective viscosity and the relative role of body forces. For instance, *Flesch et al*. [2000] used the ratio of stress to strain rate to estimate effective viscosity. Higher values of ΔGPE than used in that paper, such as in the eastern Sierra and parts of the Basin and Range would produce higher effective viscosities than published estimates and further reinforce the importance of body forces in these areas while lower GPE values, such as in the southern Rockies relative to *Flesch et al*.'s [2007] estimate, would tend to yield lower effective viscosities but would reduce the significance of GPE in driving deformation in the region.

8. Conclusions

We have generated a density model of the western U.S. lithosphere from surface heat flow and seismic models at the well-distributed Transportable Array stations and quantitatively checked it against predicted topography and gravity. Large overestimates of elevation (>600 m) near Yellowstone and in the southern Rocky Mountains are attributed to the presence of lithospheric melt, while we attribute some underestimates of topography to anomalously quartz-rich crust. Overestimated elevations near the Cascadia subduction zone probably are caused by dynamic effects up to ~1 km. Correcting for these effects yields our final density structure.

The origin of topographic variations within the western U.S. can be examined by decomposing the elevation field into its five components: crustal thermal, mantle thermal, crustal compositional, mantle compositional, and dynamic topography (Figure 6). Crustal composition (Figure 6f) and mantle temperatures (Figure 6h) dominate both in magnitude and heterogeneity. Dynamic topography (Figure 6i) is only locally important along the plate boundary, whereas crustal thermal topography (Figure 6e) is of low magnitude across the region. We find no statistically significant need for relief generated by variations in mantle composition, though variations of several hundred meters are possible.

The Cordillera overlies nearly constant density mantle (Figures 6g, 6h), and topographic relief generally reflects variations in crustal thickness and chemistry.

The Wyoming craton overlies cold, dense mantle (Figure 6h), but thick crust (Figure 1b) allows modest elevations. High velocities observed below 150 km [e.g., *Burdick et al*., 2008] presumably record cold mantle that is either itself isopycnic with surrounding asthenosphere or requires the mantle lithosphere above 150 km to be depleted and less dense than we infer here. Elevation decreases eastward into the Great Plains are due to chemically denser crust (Figure 8).

Away from the Cascadia subduction zone, our results limit topographic effects of dynamic stresses to under a few hundred meters. Our seismologically based density structure reproduces elevations within 600 m at the 2σ level. Significant dynamic effects should produce large errors in our predicted gravity field, but the differences between observed and predicted gravity are as expected from seismologically derived uncertainties.

Finally, we have uniformly quantified the variations in gravitational potential energy throughout the western U.S. (Figure 10). Positive GPE anomalies favor horizontal extension in the Northern Basin and Range and along the eastern front of the Sierra Nevada. Compression in the Yakima fold and thrust belt, conversely, coincides with negative anomalies.

Appendix A

We use our preferred 3-D density model—with adjustments for inferred melt and magnesium enrichment included—to calculate the Bouguer gravity anomaly. This model has nodes every 1 km in depth to 15 km below sea level, every 5 km from 15 to 50 km depth and every 10 km to 150 km depth. We interpolate the density estimates at all stations to a uniform grid with 65 km horizontal spacing. To broadly mitigate edge

effects and computational artifacts, we subtract a reference structure of 2670 kg/m^3 from the station elevation to sea level (effectively reproducing the Bouguer correction), 2800 kg/m^3 from the surface to 40 km depth and 3200 kg/m^3 below that. The density structure is then represented by rectangular prisms 65 × 65 km in plan view and as thick as the node spacing at each depth.

To further limit edge effects we must consider the physiography and geology of surrounding regions. We place 50 km thick crust within the mountains north (Canadian Rockies) and south (Sierra Madre) of our model (represented by prisms of +118 kg/m^3 between 0 and 40 km and −281 kg/m^3 between 40 and 50 km depth) over our reference mantle. East of the Canadian Rockies, where elevations are ~500 m we use a 40 km crust over reference mantle (prism of +118 kg/m^3 between 0 and 40 km). No adjustment is made to the east as our model extends >300 km east of 102°W, well beyond what we show here. At the Cascadia subduction zone, we approximated the upper portion of the Juan de Fuca slab (beyond the western boundary of the seismic models) as a tabular body with a density perturbation of +200 kg/m^3, thickness of 40 km, dip of 35°, and depth of 75 km at the western edge of the study area. This body produces a signal of ~+150 mGal at its western edge that decreases eastward by roughly 30 mGal per 100 km. Southward along the coast, we approximate the Pacific Plate as a 10 km thick, 3000 kg/m^3 crust (+200 kg/m^3 1–11 km) underlain by 3200 kg/m^3 mantle (+400 kg/m^3 11–40 km) and overlain by 1 km of sea water (−1800 kg/m^3 0–1 km). This body produces a ~200 mGal anomaly that decays quickly (<100 mGal within 100 km of the coast).

Gravity is calculated by summing the contributions at each grid point from all of the prisms below the station within the model. To compare with observed gravity, we add a static term—the average of Bouguer anomaly observations—to our predicted Bouguer gravity anomalies.

Acknowledgments

Early efforts on this work were funded by NSF grant EAR-060783 and seismic model construction was supported by NSF grants EAR-0844097 and EAR-1252085. We thank Peter Molnar for an insightful review, and journal reviews by Tom Brocher and an anonymous reviewer helped clarify important points.

References

Bird, P. (1988), Formation of the Rocky Mountains, western United States: A continuum computer model, *Science*, *239*, 1501–1507.

Blackwell, D. (1983), Heat flow in the northern basin and range, in *The Role of Heat in the Development of Energy and Mineral Resources in the Northern Basin and Range Province*, Special Report 13, edited by Geothermal Resources Council, pp. 81–93.

Blakely, R. J., B. L. Sherrod, C. S. Weaver, R. E. Wells, A. C. Rohay, E. A. Barnett, and N. E. Knepprath (2011), Connecting the Yakima fold and thrust belt to active faults in the Puget Lowland, Washington, *J. Geophys. Res.*, *116*, B07105, doi:10.1029/2010JB008091.

Brocher, T. (2005), Empirical relations between elastic wavespeeds and density in the Earth's crust, *Bull. Seismol. Soc. Am.*, *95*(6), 2081–2092, doi:10.1785/0120050077.

Burdick, S., C. Li, V. Martynov, T. Cox, J. Eakins, T. Mulder, F. Vernon, G. Pavlis, and R. D. van der Hilst (2008), Upper mantle heterogeneity beneath North America from travel time tomography with global and USArray transportable array data, *Seismol. Res. Lett.*, *79*(3), 384–392, doi:10.1785/gssrl.79.3.384.

Butcher, L. (2013), Re-thinking the laramide: Investigating the role of fluids in producing surface uplift using xenolith mineralogy and geochronology, M.S. thesis, 79 pp., Univ. of Colorado, Boulder, Colo.

Catchings, R. D., and W. D. Mooney (1991), Basin and Range crustal and upper mantle strucutre, northwest to central Nevada, *J. Geophys. Res.*, *96*(B4), 6247–6267.

Christensen, N. I. (1996), Poisson's ratio and crustal seismology, *J. Geophys. Res.*, *101*(B2), 3139–3156.

Christensen, N. I., and W. D. Mooney (1995), Seismic velocity structure and composition of the continental crust: A global view, *J. Geophys. Res.*, *100*(B7), 9761–9788.

Ducea, M. N., and J. B. Saleeby (1996), Buoyancy sources for a large, unrooted mountain range, the Sierra Nevada, California: Evidence from xenolith thermobarometry, *J. Geophys. Res.*, *101*(B4), 8229–8244.

Ducea, M. N., and J. B. Saleeby (1998), A case for delamination of the deep batholithic crust beneath the Sierra Nevada, California, *Int. Geol. Rev.*, *133*, 78–93.

Eaton, G. P. (1986), A tectonic redefinition of the Southern Rocky Mountains, *Tectonophysics*, *132*(1-3), 163–193.

Eaton, G. P., R. R. Wahl, H. J. Prostka, D. R. Mabey, and M. D. Kleinkopf (1978), Regional gravity and tectonic patterns: Their relation to late Cenozoic epeirogeny and lateral spreading in the western Cordillera, in *Cenozoic Tectonics and Regional Geophysics of the Western Cordillera*, edited by R. B. Smith and G. P. Eaton, pp. 51–91, Geol. Soc. Am, Boulder, Colo.

Flesch, L. M., and C. Kreemer (2010), Gravitational potential energy and regional stress and strain rate fields for continental plateaus: Examples from the central Andes and Colorado Plateau, *Tectonophysics*, *482*, 182–192, doi:10.1016/j.tecto.2009.07.014.

Flesch, L. M., W. Holt, A. J. Haines, and B. M. Shen-Tu (2000), Dynamics of the Pacific-North American plate boundary in the western United States, *Science*, *287*(5454), 834–836, doi:10.1126/science.287.5454.834.

Flesch, L. M., W. Holt, A. J. Haines, L. X. Wen, and B. M. Shen-Tu (2007), The dynamics of western North America: Stress magnitudes and the relative role of gravitational potential energy, plate interaction at the boundary and basal tractions, *Geophys. J. Int.*, *169*(3), 866–896, doi:10.1111/j.1365-246X.2007.03274.x.

Fliedner, M. M., S. L. Klemperer, and N. I. Christensen (2000), Three-dimensional seismic model of the Sierra Nevada arc, California, and its implications for crustal and upper mantle composition, *J. Geophys. Res.*, *105*(B5), 10,899–10,921.

Gilbert, H. (2012), Crustal structure and signatures of recent tectonism as influenced by ancient terranes in the western United States, *Geosphere*, *8*(1), 141–157, doi:10.1130/GES00720.1.

Goff, J. A., K. Holliger, and A. Levander (1994), Modal fields: A new method for characterization of random seismic velocity heterogeneity, *Geophys. Res. Lett.*, *21*(6), 493–496.

Grand, S. P., and D. V. Helmberger (1984), Upper mantle shear structure of North America, *Geophys. J. R. Astron. Soc.*, *76*, 399–438.

Hacker, B. R., and G. A. Abers (2004), Subduction factory 3: An Excel worksheet and macro for calculating the densities, seismic wave speeds, and H2O contents of minerals and rocks at pressure and temperature, *Geochem. Geophys. Geosyst.*, *5*, Q01005, doi:10.1029/2003GC000614.

Hammond, W. C., and E. Humphreys (2000), Upper mantle seismic velocity: Effects of realistic partial melt geometries, *J. Geophys. Res.*, *105*(B5), 10,975–10,986.
Hasterok, D. P., and D. S. Chapman (2007a), Continental thermal isostasy: 1. Methods and sensitivity, *J. Geophys. Res.*, *112*, B06414, doi:10.1029/2006JB004663.
Hasterok, D. P., and D. S. Chapman (2007b), Continental thermal isostasy: 2. Application to North America, *J. Geophys. Res.*, *112*, B06415, doi:10.1029/2006JB004664.
Haxby, W. F., and D. L. Turcotte (1978), On isostatic geoid anomalies, *J. Geophys. Res.*, *83*(B11), 5473–5478.
Holbrook, W. S. (1990), The crustal structure of the northwestern Basin and Range Province, Nevada, from wide-angle seismic data, *J. Geophys. Res.*, *95*(B13), 21,843–21,869.
Holliger, K., and A. Levander (1992), A stochastic view of the lower crust based on the Ivrea zone, *Geophys. Res. Lett.*, *19*(11), 1153–1156.
Humphreys, E. (2009), Relation of flat subduction to magmatism and deformation in the western USA, *Mem. Geol. Soc. Am.*, *204*, 85–98, doi:10.1130/2009.1204(04).
Humphreys, E., and D. Coblentz (2007), North American dynamics and western US tectonics, *Rev. Geophys.*, *45*, RG3001, doi:10.1029/2005RG000181.
Jackson, I., and U. H. Faul (2010), Grainsize-sensitive viscoelastic relaxation in olivine: Towards a robust laboratory-based model for seismological application, *Phys. Earth Planet. Inter.*, *183*, 151–163, doi:10.1016/j.pepi.2010.09.005.
Jones, C. H., J. Unruh, and L. J. Sonder (1996), The role of gravitational potential energy in active deformation in the southwestern United States, *Nature*, *381*, 37–41.
Jones, C. H., K. H. Mahan, and G. L. Farmer (2011), Post-laramide epiorogeny through crustal hydration?, Abstract T11B-2308 presented at 2011 Fall Meeting, *AGU, EOS Trans, 92*.
Karlstrom, K. E., S. J. Whitmeyer, K. G. Dueker, M. L. Williams, S. A. Bowring, A. Levander, E. D. Humphreys, and G. R. Keller (2005), Synthesis of results from the CD-ROM experiment: 4-D image of the lithosphere beneath the Rocky Mountains and implications for understanding the evolution of continental lithosphere, in *The Rocky Mountain Region—An Evolving Lithosphere*, AGU geophysical monograph, edited by K. E. Karlstrom and G. R. Keller, 421–441, AGU, Washington, D. C.
Karlstrom, K. E., et al. (2012), Surface response to mantle convection beneath the Colorado Rocky Mountains and Colorado Plateau, *Lithosphere*, *4*(1), *3*-22, doi:10.1130/L150.1.
Lachenbruch, A. H., and P. Morgan (1990), Continental extension, magmatism and elevation; formal relations and rules of thumb, *Tectonophysics*, *174*, 39–62.
Levander, A., and M. S. Miller (2012), Evolutionary aspects of the lithosphere discontinuity structure in the western U.S, *Geochem. Geophys. Geosyst.*, *13*, Q0AK07, doi:10.1029/2012GC004056.
Levander, A., B. Schmandt, M. S. Miller, K. Liu, K. E. Karlstrom, R. S. Crow, C.-T. A. Lee, and E. Humphreys (2011), Continuing Colorado plateau uplift by delamination-style convective lithospheric downwelling, *Nature*, *472*, 461–465, doi:10.1038/nature10001.
Levander, A. R., and K. Holliger (1992), Small-scale heterogeneity and large-scale velocity structure of the continental crust, *J. Geophys. Res.*, *97*(6), 8797–8804.
Levandowski, W. B., C. H. Jones, L. Butcher, and K. H. Mahan (2013a), Uplift of the Colorado Plateau by lithospheric removal and minor crustal hydration: Insights from quantitative density models, GSA Annual Meeting, Denver, Colo.
Levandowski, W. B., C. H. Jones, H. Reeg, A. Frassetto, H. Gilbert, G. Zandt, and T. J. Owens (2013b), Seismological estimates of means of isostatic support of the Sierra Nevada, *Geosphere*, *9*(6), 1552–1561, doi:10.1130/GES00905.1.
Liu, L., and M. Gurnis (2010), Dynamic subsidence and uplift of the Colorado Plateau, *Geology*, *38*(7), 663–666, doi:10.1130/G30624.1.
Livaccari, R. F., and F. V. Perry (1993), Isotopic evidence for preservation of Cordilleran lithospheric mantle during the Sevier-Laramide orogeny, western United States, *Geology*, *21*(8), 719–722.
Lowry, A. R. (2012), Estimates of effective elastic thickness (Te); surface heat flow data. [Available at http://129.123.73.40/~arlowry/Data/WUS2000/README.html, accessed 10/10/2012].
Lowry, A. R., and M. Perez-Gussinye (2011), The role of crustal quartz in controlling Cordilleran deformation, *Nature*, *471*, 353–357, doi:10.1038/nature09912.
Lowry, A. R., N. M. Ribe, and R. B. Smith (2000), Dynamic elevation of the Cordillera, western United States, *J. Geophys. Res.*, *105*(B10), 23,371–23,390.
Marone, F., Y. C. Gung, and B. Romanowicz (2007), High resolution 3D radial anisotropic structure of the North American upper mantle from inversion of surface waveform data, *Geophys. J. Int.*, *171*, 206–222, doi:10.1111/j.1365-246X.2007.03465.x.
McQuarrie, N., and C. G. Chase (2000), Raising the Colorado Plateau, *Geology*, *28*, 91–94.
Mooney, W., and M. K. Kaban (2010), The North American upper mantle: Density, composition, and evolution, *J. Geophys. Res.*, *115*, B12424, doi:10.1029/2010JB000866.
Morgan, P. (2003), Colorado plateau and southern Rocky Mountains uplift and erosion, in *Cenozoic Systems of the Rocky Mountain Region*, edited by R. G. Reynolds, SEPM, Tulsa, Okla., 43 pp.
Morgan, P., and W. D. Gosnold (1989), Heat flow and thermal regimes in the continental United States, in *Geophysical Framework of the Continental United States*, edited by L. C. Pakiser and W. D. Mooney, pp. 493–522, Geol. Soc. Am., Boulder, Colo.
Moschetti, M. P., M. H. Ritzwoller, F. C. Lin, and Y. Yang (2010), Seismic evidence for widespread western-US deep-crustal deformation caused by extension, *Nature*, *464*, 885–889, doi:10.1038/nature08951.
Moucha, R., A. M. Forte, D. B. Rowley, J. X. Mitrovica, G. Simmons, and S. P. Grand (2008), Mantle convection and recent evolution of the Colorado Plateau and the Rio Grande Rift Valley, *Geology*, *36*(6), 439–442, doi:10.1130/G24577A.
Parsons, B., and S. Daly (1983), The relationship between surface topography, gravity anomalies, and temperature structure of convection, *J. Geophys. Res.*, *88*(B02), 1129–1144.
Parsons, T., and W. R. Thatcher (2011), Diffuse Pacific-North American plate boundary: 1000 km of dextral shear inferred from modeling geodetic data, *Geology*, *39*(10), 943–946, doi:10.1130/G32176.1.
Payne, S. J., R. McCaffrey, and S. A. Kattenhorn (2013), Extension-driven right-lateral shear in the centennial shear zone adjacent to the eastern Snake River Plain, Idaho, *Lithosphere*, *5*(4), 407–419, doi:10.1130/L200.1.
Phillips, W. S., and R. J. Stead (2008), Attenuation of Lg in the western US using the USArray, *Geophys. Res. Lett.*, *35*, L07307, doi:10.1029/2007GL032926.
Prodehl, C. (1979), *Crustal Structure of the Western United States*, U. S. Geol. Surv. Prof. Pap., vol. 1034, 74 pp.
Pysklywec, R. N., and J. X. Mitrovica (1997), Mantle avalanches and the dynamic topography of continents, *Earth Planet. Sci. Lett.*, *148*(3-4), doi:10.1016/S0012-821X(97)00045-9.
Roy, M., T. H. Jordan, and J. Pederson (2009), Colorado Plateau magmatism and uplift by warming of heterogeneous lithosphere, *Nature*, *459*, 978–982, doi:10.1038/nature08052.

Saleeby, J. (2003), Segmentation of the Laramide slab—Evidence from the southern Sierra Nevada region, *Geol. Soc. Am. Bull.*, *115*(6), 655–668.

Saltus, R. W., and A. H. Lachenbruch (1991), Thermal evolution of the Sierra Nevada; tectonic implications of new heat flow data, *Tectonics*, *10*(2), 325–344.

Saltus, R. W., and G. A. Thompson (1995), Why is it downhill from Tonopah to Las Vegas? A case for mantle plume support of the high northern Basin and Range, *Tectonics*, *14*, 1235–1244.

Schmandt, B., and E. Humphreys (2010), Complex subduction and small-scale convection revealed by body wave tomography of the western U.S. upper mantle, *Earth Planet. Sci. Lett.*, *297*, 435–445.

Schulte-Pelkum, V., G. P. Biasi, A. F. Sheehan, and C. H. Jones (2011), Differential motion between upper crust and lithospheric mantle in the central Basin and Range, *Nat. Geosci.*, *4*, 619–623, doi:10.1038/NGEO1229.

Schutt, D., and C. E. Lesher (2010), Compositional trends among Kaapvaal Craton garnet peridotite xenoliths and their effects on seismic velocity and density, *Earth Planet. Sci. Lett.*, *300*, 367–373, doi:10.1016/j.epsl.2010.10.018.

Schutt, D., J. Buehler, K. G. Dueker, and A. R. Lowry (2011), Lithopsheric temperatures in the western U.S., Institute on the Lithosphere Asthenosphere Boundary, Portland, OR, Sep. 19–21.

Shen, W., M. Ritzwoller, and V. Schulte-Pelkum (2013a), A 3-D model of the crust and uppermost mantle beneath the central and western US by joint inversion of receiver functions and surface wave dispersion, *J. Geophys. Res. Solid Earth*, *118*, 262–276, doi:10.1029/2012JB009602.

Shen, W., M. Ritzwoller, V. Schulte-Pelkum, and F. C. Lin (2013b), Joint inversion of surface wave dispersion and receiver functions: A Bayesian Monte-Carlo approach, *Geophys. J. Int.*, *192*, 807–836, doi:10.1093/gji/ggs050.

Sigloch, K., and M. G. Mihalynuk (2013), Intra-oceanic subduction shaped the assembly of Cordilleran North America, *Nature*, *496*, 50–56, doi:10.1038/nature12019.

Southern Methodist University (SMU) (2012), SMU geothermal laboratory surface heat flow. [Available at http://smu.edu/geothermal/georesou/DataRequest.asp, accessed 11/15/2012].

Sonder, L. J., and C. H. Jones (1999), Western United States extension: How the west was widened, *Annu. Rev. Earth Planet. Sci.*, *27*, 417–462.

Spencer, J. E. (1996), Uplift of the Colorado Plateau due to lithosphere attenuation during Laramide low-angle subduction, *J. Geophys. Res.*, *101*(B6), 13,595–13,609.

Unruh, J., and E. Hauksson (2009), Seismotectonics of an evolving intracontinental plate boundary, southeastern California, *Spec. Pap. Geol. Soc. Am.*, *447*, 351–372, doi:10.1130/2009.2447(16).

Watts, A. B. (2001), *Isostasy and Flexure of the Lithosphere*, 458 pp., Cambridge Univ. Press, Cambridge, U. K.

Wolf, L. W., and J. J. Cipar (1993), Through thick and thin: A new model for the Colorado Plateau from seismic refraction data from Pacific to Arizona crustal experiment, *J. Geophys. Res.*, *98*(11), 19,881–19,894.